Growth Mechanisms of Mesoscale Prussian Blue Analogue Particles in Modifier-free Synthesis

Jiamin Liang, Carissa H. Li, Daniel R. Talham

Department of Chemistry, University of Florida, Gainesville, FL 32611-7200, United States

Corresponding author: Daniel R. Talham

Phone: 352-392-9016

E-mail: talham@chem.ufl.edu

Abstract

The growth mechanism of mesoscale, 100 nm – 500 nm, Prussian blue analogue (PBA) particles synthesized via a modifier-free co-precipitation method has been investigated. A series of Co^{2+} and Ni^{2+} analogues, $Rb_jCo_k[M(CN)_6]_l \bullet nH_2O$ (M = Cr, Fe, Co) and $Rb_jNi_k[M(CN)_6]_l \bullet nH_2O$ (M = Cr, Fe, Co) are compared, along with the parent Prussian blue and the Cu^{2+} analogue, rubidium copper hexacyanoferrate. The study finds that growth mechanisms differ among this closely related family of compounds. *Ex situ* TEM and *in situ* ionic conductivity and DLS analyses indicate the Cu^{2+} and Ni^{2+} analogues grow by a traditional heterogeneous precipitation process whereby nucleated particles grow by addition of ions from solution. On the other hand, the Co^{2+} analogues and the parent rubidium ferric ferrocyanide grow by aggregation of precursor particles followed by annealing into crystalline mesoscale particles. Understanding of the growth mechanisms is useful for designing routes to mesoscale coordination polymer structures and heterostructures.

Introduction

Prussian blue and the mixed metal Prussian blue analogues (PBA's) of general formula $A_jM'_k[M(CN)_6]_l \bullet nH_2O$ (A = monovalent cation, M' = divalent transition metal, and M = trivalent transition metal) are three dimensional coordination polymer networks widely studied in areas that include electrochromism,[1, 2] photoimage formation,[3] ion-exchange,[4, 5] ion-sensing,[6] electrocatalysis,[7] photoelectrochemistry and photocatalysis,[8, 9] batteries,[10-15] as well as synthetic magnets and photomagnetism.[16, 17] More recently, there is significant interest in how the behavior of these simple but fascinating networks changes at the nanoscale and mesoscale.[18] While Prussian blue has long been known to form as nanoscale colloidal particles that aggregate to different degrees depending on synthetic conditions, more general efforts aimed at purposefully controlling the size and morphology of Prussian blue and PBA particles generally started with microemulsion methods, whereby surfactants modifying the particle surface limit growth and aggregation.[19-21] Similar concepts using polymer[22-24] or molecular[25] modifiers have also been found to be successful routes to stable Prussian blue and PBA nanoparticles. A recent comprehensive review describes these and other examples of PBA particles.[18]

In some applications, the presence of surface binding groups is unwanted, as they may influence physical behavior or hinder subsequent modification when targeting core-shell particles or more complex heterostructures. To address this issue, Catala and Mallah and coworkers[26,27] developed a surface modifier-free route to charge-stabilized suspensions of unmodified PBA particles. Under appropriate conditions, nanometer scale particles are formed with sufficient surface charge to avoid aggregation. These authors also showed how the modifier free suspensions can serve as seeds for the subsequent addition of further precursor to grow larger size-controlled particles or for the epitaxial growth of a shell of a different PBA.[18, 28, 29] How the chemistry and growth conditions influence the kinetics and morphology of these charge-stabilized PBA nanoparticles has been carefully explored.[18]

We and others have adapted the Catala method to achieve PBA particles and core-shell heterostructures on the 100 nm to 500 nm size regime for studies on battery cathodes,[11, 30, 31] magnetism

and light-induced magnetism,[32-40] and elastic effects in solid-state spin transitions.[40,41] While details of how the nanometer scale particles grow were described by Catala and Mallah and coworkers,[18] the mechanism of how the larger mesoscale PBA particles form in the absence of surface modifiers has not been elucidated. Better understanding of the growth mechanisms at the mesoscale can influence the design and synthesis of more complex structures at these length scales. The present study monitors the growth of two series of mesoscale PBA's, $Rb_jCo_k[M(CN)_6]_l \bullet nH_2O$ (M = Cr, Fe, Co) and $Rb_jNi_k[M(CN)_6]_l \bullet nH_2O$ (M = Cr, Fe, Co) and finds two different behaviors for the Co^{2+} and Ni^{2+} hexacyanometallates (the article uses the shorthand RbCoM-PBA and RbNiM-PBA for these two series). Mesoscale particles in the Co^{2+} series clearly grow through the aggregation and annealing of smaller precursor particles. On the other hand, evidence for precursor particles is not seen in the Ni^{2+} series, which, on the timescales studied, shows behavior more in line with a classical crystal growth mechanism. Two other examples, Prussian blue itself and the PBA $Rb_jCu_k[Fe(CN)_6]_l \bullet nH_2O$ (RbCuFe-PBA), are also compared under the same growth conditions used for the Co^{2+} and Ni^{2+} series.

Experimental section

Synthesis and isolation methods.

All chemical reagents are purchased from Sigma-Aldrich and used without further purification. All syntheses and characterizations are performed at room temperature. Particle samples were isolated using a Thermo Scientific Sorvall Legend X1 centrifuge. Sampling during a reaction employed a Thermo Scientific Microliter 30x2 sealed rotor and Fisherbrand 1.5 mL premium microcentrifuge tubes, resulting in 9916 g as the maximum relative centrifugal force (RCF) from 10,000 rpm. Final products were isolated using a Thermo Scientific FIBERLiteTM F15- 6x100 rotor and Fisherbrand Higher-Speed 50mL Easy Reader plastic centrifuge tubes, resulting in 8229 g as the maximum RCF from 10,000 rpm.

Synthesis of PBA particles by slow addition of the precursors.

The coprecipitation method was used to synthesize PBA particles.[18, 26, 28, 29, 42, 43] Each system was

synthesized by simultaneous addition of a 100 mL aqueous solution of the mixture of 4.0 mM $MCl_2 \cdot nH_2O$ (M = Fe, Co, Ni, Cu) and 8.0 mM RbCl, along with a 100 mL aqueous solution of 4.5 mM $K_3[M'(CN)_6]$ (M' = Cr, Fe, Co) to 200 mL nano-pure water at a rate of 1 mL/min via peristaltic pump. At the end of the slow addition process, the resulting 400 mL solution contained 1.0 mM $MCl_2 \cdot nH_2O$ (M = Fe, Co, Ni, Cu), 2.0 mM RbCl and 1.1 mM $K_3[M'(CN)_6]$ (M' = Cr, Fe, Co). Vigorous stirring was maintained during and after the addition process and continued overnight. Samples were isolated via high speed centrifugation (10000 rpm, 10 minutes) and washed with nano-pure water before further characterization. Particle sizes were measured using TEM images and the corresponding particle size vs number histograms are included in Supporting Information.

$Rb_{0.2}Ni[Fe(CN)_6]_{0.7} \bullet nH_2O$ (**RbNiFe PBA)**. Particle size: 125 ± 28 nm. Dark yellow powder. IR (KBr): 2168 cm^{-1} ($\tilde{\upsilon}$CN, Ni^{II}–NC–Fe^{III}), 2102 cm^{-1} ($\tilde{\upsilon}$CN, Ni^{II}–NC–Fe^{II}). EDS atomic% (Rb/Ni/Fe): 7.8/51.7/40.5.

$Rb_{0.2}Ni[Cr(CN)_6]_{0.7} \bullet nH_2O$ (**RbNiCr PBA)**. Particle size: 98 ± 17 nm. Light blue-green powder. IR (KBr): 2174 cm^{-1} ($\tilde{\upsilon}$CN, Ni^{II}–NC–Cr^{III}). EDS atomic% (Rb/Ni/Cr): 9.4/49.5/36.1.

$Rb_{0.2}Ni[Co(CN)_6]_{0.7} \bullet nH_2O$ (**RbNiCo PBA)**. Particle size: 71 ± 12 nm. Light blue powder. IR (KBr): 2182 cm^{-1} ($\tilde{\upsilon}$CN, Ni^{II}–NC–Co^{III}). EDS atomic% (Rb/Ni/Co): 10.0/52.0/38.0.

$Rb_{0.2}Co[Fe(CN)_6]_{0.7} \bullet nH_2O$ (**RbCoFe PBA)**. Particle size: 420 ± 55 nm. Dark purple powder. IR (KBr): 2161 cm^{-1} ($\tilde{\upsilon}$CN, Co^{II}(HS)–NC–Fe^{III}), 2109 cm–1 ($\tilde{\upsilon}$CN, Co^{III}(LS)–NC–Fe^{II}), and 2095 cm^{-1} ($\tilde{\upsilon}$CN, Co^{II}–NC–Fe^{II}). EDS atomic% (Rb/Co/Fe): 13.6/49.9/36.5.

$Rb_{0.2}Co[Cr(CN)_6]_{0.7} \bullet nH_2O$ (**RbCoCr PBA)**. Particle size: 541 ± 89 nm. Light pink powder. IR (KBr): 2169 cm^{-1} ($\tilde{\upsilon}$CN, Co^{II}–NC–Cr^{III}). EDS atomic% (Rb/Co/Cr): 12.5/52.9/34.6.

$Rb_jCo[Co(CN)_6]_l \bullet nH_2O$ (**RbCoCo PBA)**. Particle size: 553 ± 96 nm. Pink powder. IR (KBr): 2175 cm^{-1} ($\tilde{\upsilon}$CN, Co^{II}–NC–Co^{III}).

$Rb_jFe[Fe(CN)_6]_l \bullet nH_2O$ (**Prussian blue**). Particle size: 39 ± 5 nm. Dark blue powder. IR (KBr): 2082 cm^{-1} ($\tilde{\upsilon}$CN, Fe^{III}–NC–Fe^{II}).

$Rb_jCu[Fe(CN)_6]_l \bullet nH_2O$ (**RbCuFe PBA)**. Particle size: 194 ± 109 nm. Dark yellowish brown powder. IR (KBr):

2103 cm^{-1} ($\tilde{\nu}$CN, Cu^{II}–NC–Fe^{III}).

Synthesis of PBA nanoparticles by fast mixing of precursors.

PBA nanoparticles were also synthesized by the immediate simultaneous addition of an 8 mL aqueous solution containing 4.0 mM $MCl_2 \cdot nH_2O$ (M = Fe, Co, Ni, Cu) (32 µmol) and 8.0 mM RbCl (64 µmol) plus an 8 mL aqueous solution of 4.5 mM $K_3[M'(CN)_6]$ (M' = Cr, Fe, Co) (36 µmol) to 400 mL nano-pure water. At the end of the fast addition process, the resulting 416 mL solution contained 0.077 mM $MCl_2 \cdot nH_2O$ (M = Fe, Co, Ni, Cu), 0.15 mM RbCl and 0.087 mM $K_3[M'(CN)_6]$ (M' = Cr, Fe, Co). Vigorous stirring was maintained overnight and particles were isolated using centrifugation, as described, above.

$Rb_{0.2}Ni[Fe(CN)_6]_{0.7} \bullet nH_2O$ (RbNiFe PBA). Particle size: 57 ± 12 nm (DLS number distribution). Dark yellow powder. IR (KBr): 2168 cm^{-1} ($\tilde{\nu}$CN, Ni^{II}–NC–Fe^{III}), 2101 cm^{-1} ($\tilde{\nu}$CN, Ni^{II}–NC–Fe^{II}). EDS atomic% (Rb/Ni/Fe): 8.7/53.4/37.9.

$Rb_jNi[Cr(CN)_6]_l \bullet nH_2O$ (RbNiCr PBA). Particle size: 297 ± 104 nm (DLS number distribution). Light blue-green powder. IR (KBr): 2174 cm^{-1} ($\tilde{\nu}$CN, Ni^{II}–NC–Cr^{III}).

$Rb_{0.2}Ni[Co(CN)_6]_{0.7} \bullet nH_2O$ (RbNiCo PBA).Particle size: 77 ± 18 nm (DLS number distribution). Light blue powder. IR (KBr): 2182 cm^{-1} ($\tilde{\nu}$CN, Ni^{II}–NC–Co^{III}). EDS atomic% (Rb/Ni/Co): 8.5/53.2/38.3.

$Rb_{0.2}Co[Fe(CN)_6]_{0.7} \bullet nH_2O$ (RbCoFe PBA). Particle size: 165 ± 37 nm (DLS number distribution); 186 ± 18 nm (TEM). Dark purple powder. IR (KBr): 2161 cm^{-1} ($\tilde{\nu}$CN, Co^{II}(HS)–NC–Fe^{III}), 2109 cm–1 ($\tilde{\nu}$CN, Co^{III}(LS)–NC–Fe^{II}), and 2094 cm^{-1} ($\tilde{\nu}$CN, Co^{II}–NC–Fe^{II}). EDS atomic% (Rb/Co/Fe): 9.6/50.8/39.6.

$Rb_jCo[Cr(CN)_6]_l \bullet nH_2O$ (RbCoCr PBA). Particle size: 28 ± 9 nm (DLS number distribution) ; 221 ± 104 nm (78%), Light pink powder. IR (KBr): 2169 cm^{-1} ($\tilde{\nu}$CN, Co^{II}–NC–Cr^{III}).

$Rb_jCo[Co(CN)_6]_l \bullet nH_2O$ (RbCoCo PBA). Particle size: 577 ± 187 nm (DLS number distribution). Pink powder. IR (KBr): 2175 cm^{-1} ($\tilde{\nu}$CN, Co^{II}–NC–Co^{III}).

$Rb_jFe[Fe(CN)_6]_l \bullet nH_2O$ (**Prussian blue**). Particle size: 51 ± 19 nm (DLS number distribution). Dark blue powder. IR (KBr): 2082 cm^{-1} ($\tilde{\upsilon}$CN, Fe^{III}–NC–Fe^{II}).

$Rb_jCu[Fe(CN)_6]_l \bullet nH_2O$ (**RbCuFe PBA)**. Particle size: 65 ± 22 nm (DLS number distribution). Dark yellowish brown powder. IR (KBr): 2103 cm^{-1} ($\tilde{\upsilon}$CN, Cu^{II}–NC–Fe^{III}).

Characterization methods.

Transmission electron microscopy (TEM) was performed on a JEOL-200CX low-resolution transmission electron microscope at 200 kV, and a JEOL 2010F high-resolution transmission electron microscope at 200 kV equipped with the Oxford INCA Si(Li) energy dispersive spectroscopy (EDS) system. The TEM samples were prepared by dropping 50 µL of an aqueous solution containing PBA nanoparticles, dispersed by sonication, onto the grid (carbon film on a holey carbon support film, 400 mesh, copper from Ted-Pella, Inc.). Conductance measurements were performed using a YSI 3200 conductivity meter with a YSI 3253 conductivity cell. Dynamic light scattering measurements were performed on a Zetasizer Nano particle characterization system using a 173° angle of detection. For *ex situ* measurements, isolated PBA nanoparticles were dispersed in water then filtered into disposable cuvettes DTS0012 (Polystyrene latex, Refractive index (RI) = 1.590, Absorption = 0.010) via 0.45µm filter. For *in situ* measurements, immediately following the mixing of precursors, a 1.5 mL sample was filtered into the disposable cuvette and the reaction continuously monitored. Infrared spectra (IR) were performed on a Nicolet 6700 Thermo Scientific spectrophotometer. Samples were prepared by mixing 2 mg of powder samples with 100 mg KBr and pressing into a pellet at 3000 PSI. The chemical identity of each nanoparticle sample was confirmed by comparing frequencies to published data.[44] Chemical formulas were assigned based on EDS elemental ratios. Exact water content was not determined.

Results

Mesoscale PBA particles using a slow addition of precursors

Prussian blue analogue particles with controllable uniform size are typically prepared by the gradual addition of divalent metal and cyanometallate precursors to water or a water/alcohol mixture followed by continuous stirring for a period of hours.[18, 26, 28, 29, 42, 43] In the present study this procedure is called the slow addition of precursors, and reactants were combined over 100 min. to achieve approximately 1 mM concentration of precursor ions followed by continued stirring overnight before isolating particles using centrifugation. Figure 1 compares particles for several common PBA's formed in this way based on divalent Ni^{2+} or divalent Co^{2+} with different cyanometallates. In each case particles with well-defined faces in the 100 nm-500 nm size regime are formed. Although the final products of the different analogues have very similar appearance, significant differences are seen during the growth processes. For example, Figures 2 and 3 contrast the growth of RbNiFe-PBA and RbCoFe-PBA by isolating samples taken from the reaction at different times during the precursor addition process.

For RbNiFe PBA, the particle size significantly increased from 83 ± 12 nm at the first sampling to 124 ± 24 nm at the end of the slow addition process, where it remained until the synthesis was terminated after 24 hrs. The particles are characterized by cubic shapes with smooth faces. The growth of the RbNiCr-PBA and RbNiCo-PBAs follow similar patterns, as show in the Supporting Information, Figures SI1 – SI6.

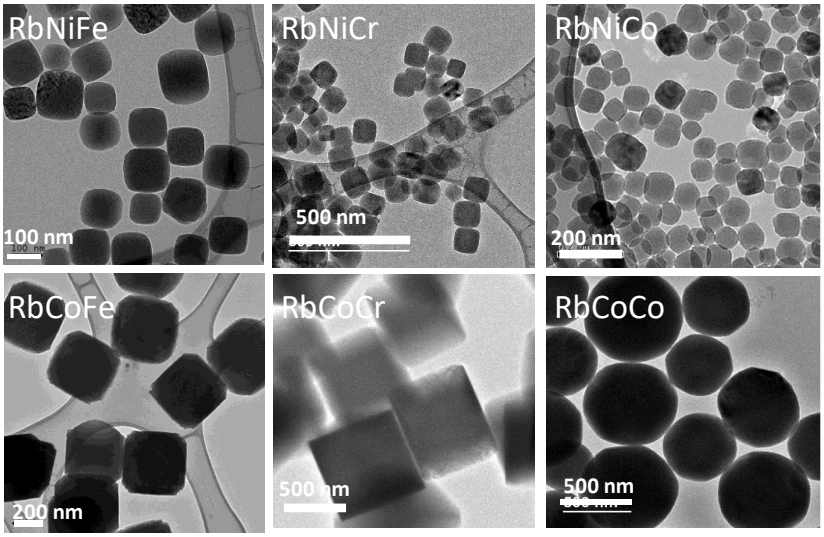

Figure 1. TEM images of mesoscale particles of the nickel hexacyanometallate (top row) and cobalt hexacyanometallate (bottom row) series prepared using the slow addition of precursors method described in the text.

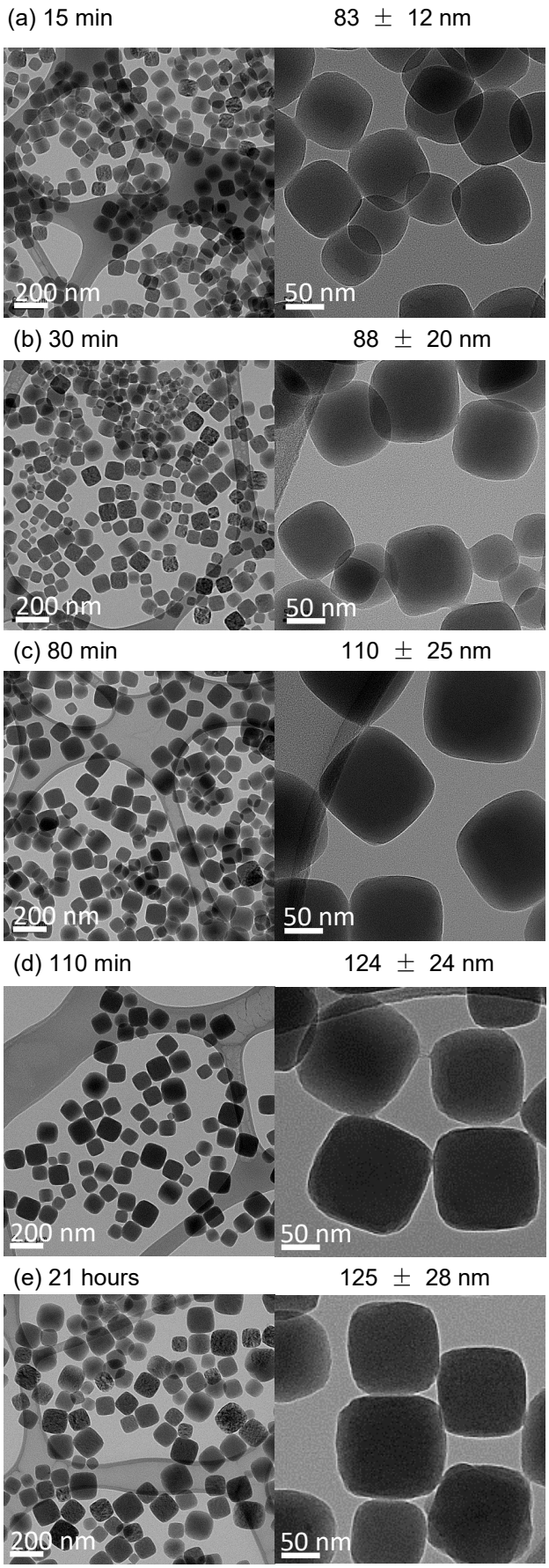

Figure 2. TEM micrographs monitoring the growth of RbNiFe-PBA particles prepared using the slow addition of precursors synthetic method described in the text. Samples for imaging are extracted from the same synthetic batch at the times indicated. The particle size and size distributions are determined from the corresponding histograms which appear in Supporting Information.

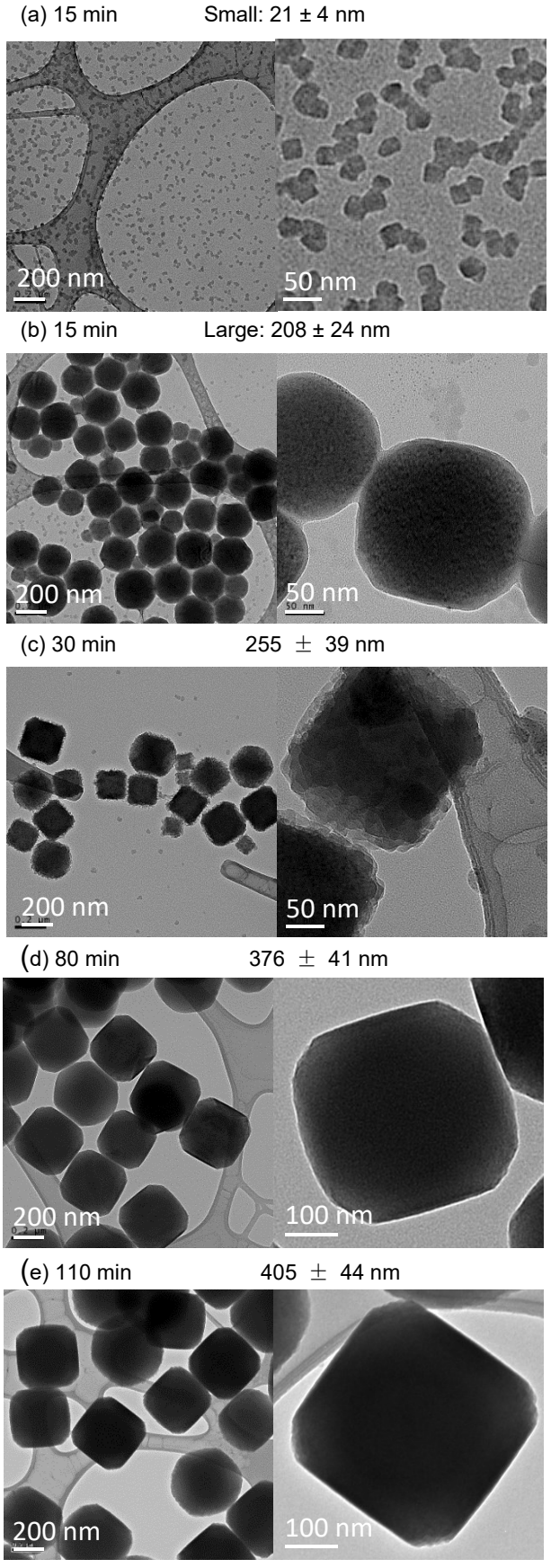

Figure 3. TEM micrographs monitoring the growth of RbCoFe-PBA particles prepared using the slow addition of precursors synthetic method described in the text. Samples for imaging are extracted from the same synthetic batch at the times indicated. At early times both large and small particles are observed, as shown in a and b after 15 minutes. Both images are from the same grid, taken of regions where there are only smaller particles (a) and where both large and small particles are present (b). The particle size and size distributions are determined from the corresponding histograms which appear in Supporting Information.

On the other hand, the growth of the RbCoFe-PBA particles appears very different, Figure 3. At the first sampling, after 15 min, there are cubic particles with average size 208 ± 24 nm that grow to 420 ± 55 nm by the end of the synthesis. However, in addition to these larger particles, an abundance of smaller particles with size 21 ± 4 nm can be observed as background at early times. Further, close inspection of the faces of the larger particles early in the growth shows them to be aggregates of the smaller particle building blocks. Later in the process the small particles are no longer evident and faces on the larger particles gradually become smoother. The growth of the RbCoCr-PBA and RbCoCo-PBA particles show similar features (Supporting Information Figures SI7 – SI12) with small particle or amorphous precipitates observed alongside larger particles at early growth times evolving into well-defined particles with smooth faces by the end of the synthesis. At least at the early stages of growth, mesoscale particles of the Co^{2+} PBA's appear to form through the initial aggregation of smaller precursor objects.

Mesoscale PBA particles by fast mixing of precursors

To gain further insights into the growth processes, the synthetic procedure was changed to instantaneously add all precursors, thereby allowing observations on the time evolution of the particle growth without the complication of continually adding reactants. In addition to the *ex situ* analysis of the particles using TEM, the time evolution of the particle growth can be monitored using *in situ* conductivity and dynamic light scattering (DLS) methods.

The results of time dependent conductance and DLS measurement during the growth of RbNiFe PBA nanoparticles are illustrated in Figure 4. The conductance monitors the change in the dissolved ion content as it evolves, first reflecting the dissolved precursors and equilibrating at values that correspond to those ions, primarily counterions, not included in the product networks. For RbNiFe-PBA, the majority of the conductance decrease occurs over about five hours before equilibrating after

about twelve hours. The DLS response is also shown in Figure 4.

Once particles are detected after a short time lag, particle size increased consistently to about 55 nm after three hours and then stabilized near 57 nm after about five hours. The time dependence of the particle growth correlates well with the change in ion concentrations monitored with the conductance measurement, keeping in mind DLS estimates a particle diameter and not the particle volume. Overall, the particle precipitation during the single addition synthesis is consistent with the observations of the

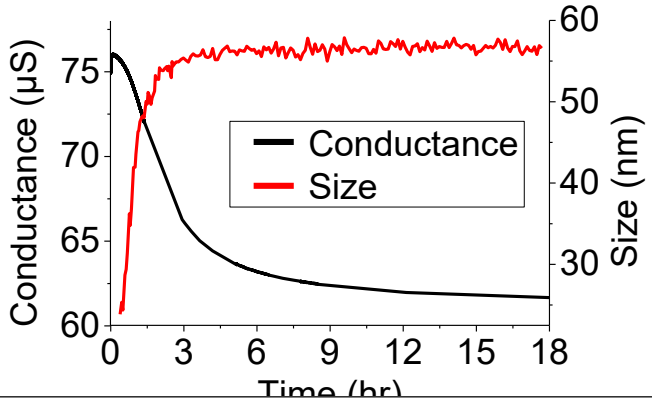

Figure 4. Time dependence of the solution conductance and DLS-determined particle size for the growth of RbNiFe-PBA particles using the fast addition of precursor method described in the text. Time = 0 corresponds to the time precursors are added to the solvent.

slow-growth experiments that the divalent nickel series of PBAs grow by building up from the addition of solution precursor ions.

The divalent cobalt PBA series was also studied using the single addition of reactants and, as for the slow addition preparation, TEM analysis shows evidence for small precursor particles which aggregate to form larger particles. Individual, 30 ± 9 nm particles with irregular shape appeared at 1 min of the RbCoFe synthesis, shown in Figure 5. Select area diffraction at this stage indicates the particles do not diffract and are largely amorphous. When the reaction time reaches 20 min, larger (82 ± 16 nm) cubic shape particles with coarse faces can be observed, evidently formed by the aggregation of the smaller particles that form initially. With time, the particles continue to grow and the faces gradually become smooth. After 24 h, uniform particles with average size 184 nm are seen for the RbCoFe-PBA synthesis.

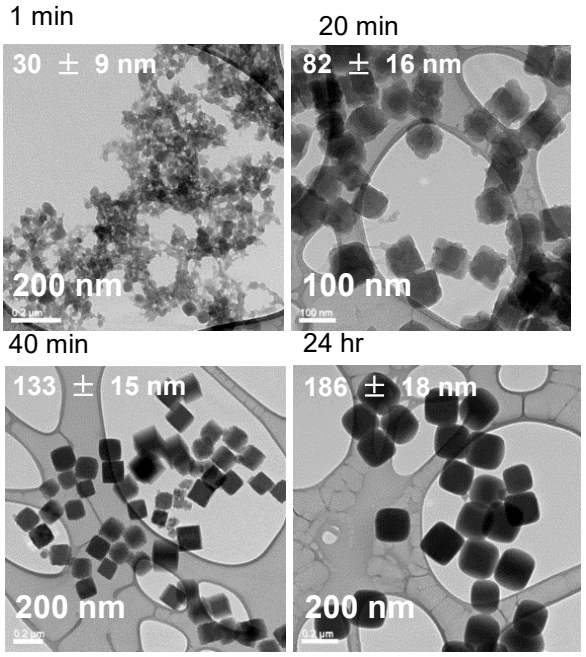

Figure 5. TEM micrographs monitoring the growth of RbCoFe-PBA particles prepared using the fast addition of precursors synthetic method.

Particle size monitoring during the RbCoFe-PBA growth using DLS is shown in Figure 6. In contrast to the case of RbNiFe-PBA, which showed a smooth evolution of the average particle size, the growth of the RbCoFe-PBA and RbCoCo-PBA are less uniform, with evidence of "steps" in the average particle size. For the first few minutes of the RbCoFe-PBA synthesis, DLS-measured particle size hovers just below 40 nm, which corresponds well to the particles imaged after 1 min. of reaction time in Figure 5. With time, the DLS size-average increases gradually. For the RbCoCo-PBA growth, steps in the growth are even more dramatic, with multiple steps observed, Figure 6. In contrast to the particle size measurements, the conductivity measurements do not show corresponding plateaus (Supporting Information) indicating that, whereas there may be steps in the evolution of the particle size, the condensation of the ions is a much more continuous process.

Discussion

Figures 2 and 3 and additional images in the Supporting Information make evident the Ni^{2+} and Co^{2+} hexacyanometallate PBA particles form at different rates and through apparently different mechanisms. Although the observations in this study are made well past the point where

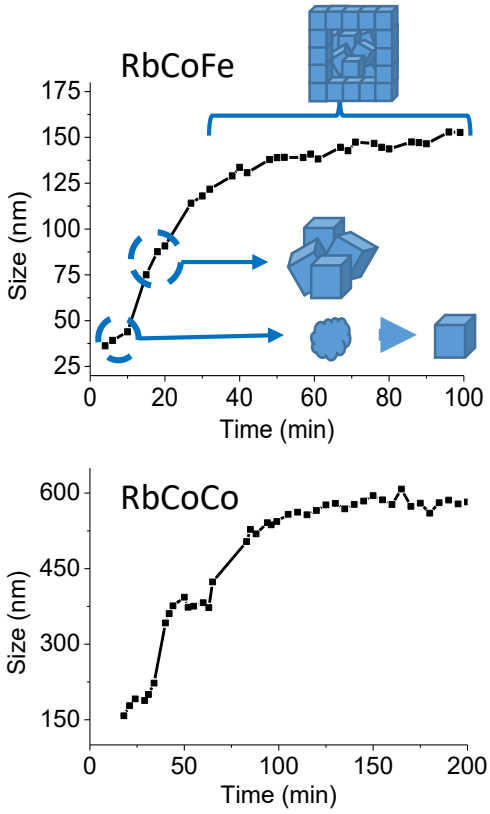

Figure 6. Time dependence of the DLS-determined particle size for the growth of RbCoFe-PBA (top) and RbCoCo-PBA (bottom) using the fast addition of precursor method described in the text. Steps in the growth correlate with the precursor particles and aggregates of particles observed in the TEM studies. Time = 0 corresponds to the time precursors are added to the solvent.

supersaturation is achieved, on the timescales monitored each of the Ni^{2+} compounds appear to follow a classical growth process with the amplification of nuclei by the continued deposition of ions from solution. On the other hand, each of the Co^{2+} PBA's follow a non-classical crystallization process[45, 46] whereby the crystallites grow through aggregation of precursor particles followed by annealing of the aggregates into crystalline particles. The precursor particles are small cubes in the slow addition synthesis, Figure 3, but lack a defined shape when formed rapidly under the single addition conditions, Figure 5. In neither case do these precursor particles diffract in the TEM indicating the initial formation of an amorphous precipitate.

These amorphous precursor particles become the building blocks of the eventual mesoscale particles, eventually fusing and annealing into crystallites. The fusing of precursor Prussian blue or Prussian blue analogue particles into larger particles or mesocrystals has previously been seen even in the presence of surface modifiers.[18, 47, 48] Examples include the recent hydrothermal preparation of Prussian blue particles[47, 49, 50] in the presence of surfactants or the assembly of citrate-modified PBA particles into larger arrays by Hu et al.[51] It is not surprising, then, that unmodified particles can aggregate into larger particles. The absence of surface modifier facilitates the particle fusion and annealing into larger homogenous particles. The annealing process is seen in eventual conversion of heterogeneous particle surfaces into smooth faces and is further seen by the evolution of contrast in TEM images, as shown in Figure 7 for RbCoFe-PBA particles formed during the single addition process, where darker and lighter regions in the bright-field images of individual particles can be seen as the structures anneal.

The different behavior of the Co^{2+} and Ni^{2+} series correlates with the difference in solubility. Figure 8 compares the initial change in conductance during particle growth for RbNiM PBA's and RbCoM PBA's (M = Co, Fe). As seen in Figure 8, the ionic concentration falls more quickly for RbCoCo-PBA and RbCoFe-PBA than for either of the Ni^{2+} PBA's, indicating more rapid precipitation. The fast condensation of the ions leads to large numbers of small particles which form without fully crystallizing, but, in the absence of surface passivating additives, can aggregate into to larger particles.

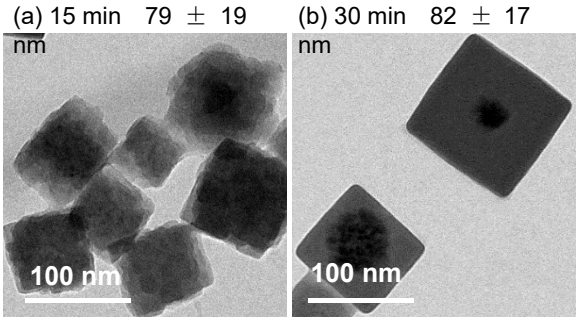

Figure 7. RbCoFe particles during the growth process showing differences in contrast within individual particles, providing evidence for annealing following the aggregation of precursor particles.

The slower change in ionic conductivity for the Ni^{2+} analogues relative to the Co^{2+} analogues is consistent with observations of Catala and cowork

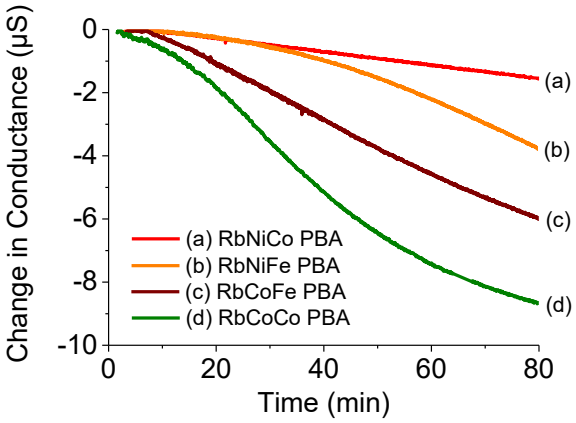

Figure 8. Comparison of the change in conductance vs time during particle growth of the nickel and cobalt hexacyanoferrates and nickel and cobalt hexacyanocobaltates. The lower solubility of the cobalt series, indicated by the faster decrease in ionic conductivity, correlates with the observation of precursor particles.

changes under similar conditions at shorter times in the presence of Cs^+ instead of Rb^+, and correlated the trend with the faster water exchange rate of aqueous Co^{2+}. However, it should be noted that under their conditions very small particles of both the nickel hexacyanoferrate and cobalt hexacyanoferrate were formed. If small, sub-20 nm, precursor particles of RbNiFe-PBA form, we were not able to detect them. However, we cannot rule out the fast formation and aggregation of such particles at times before we sampled. Nevertheless, during the RbNiFe-PBA growth stages such precursor particles are not seen and growth is consistent with growth by classical heterogeneous

precipitation.

Under the identical synthetic conditions used in this comparison, the Co^{2+}-based PBA's eventually form larger particles than the analogous Ni^{2+}-based PBA's, despite the faster precipitation of the Co^{2+} compounds. For the slow addition synthetic method, after 21 hours the system has had opportunity to equilibrate and the average size of the RbNiFe-PBA, RbNiCr-PBA and RbNiCo-PBA particles are 125 ± 28, 98± 17 nm, and 71 ± 12 nm, respectively (Figures SI1-SI6). On the other hand, for RbCoFe-PBA, RbCoCr-PBA and RbCoCo-PBA the corresponding sizes are 420 ± 55, 540± 89 nm, and 553 ± 96 nm (Figures SI7-SI12). At these long reaction times, particles have had opportunity to anneal and undergo ripening processes and the particle size is determined by equilibration of the surface energies under the conditions of the reaction media. Given the similar structures, it is likely that the generally different particle sizes for the Ni^{2+} series and Co^{2+} series is a consequence of the different growth mechanisms. The effect of the particle surface energy during a growth process involving the adsorption of precursor ions should be very different than for a process whereby nanoscopic particles or amorphous precursors aggregate.

Two other systems were studied under the same conditions and provide interesting comparisons. Prussian blue and copper hexacyanoferrate, RbCuFe-PBA, are chemically distinct from the two previous series. In Prussian blue, charge transfer results in Fe^{II}-CN-Fe^{III} linkages in contrast to the M^{III}-CN-M^{II} linkages in the other analogues, and in the RbCuFe-PBA, the Cu^{2+} coordination will deviate from octahedral, so the nucleation and growth processes are expected to show differences relative to the Ni^{2+} and Co^{2+} series. Furthermore, both have lower solubility than any of the Ni^{2+} or Co^{2+} PBA series (Supporting Information). Prussian blue is known to form nanometer scale colloidal particles and has previously been shown to undergo aggregation and annealing when larger particles are formed.[47, 49, 50] Prussian blue particles formed using the same conditions described for the other analogues in this study are characterized in Figure 9. Rapid precipitation results in randomly shaped, sub-20 nm particles. With time, these smaller particles aggregate and anneal. After 23 hours, slightly larger

cubic shapes can be seen. However, the annealing process is slow, presumably a consequence of the very low solubility.

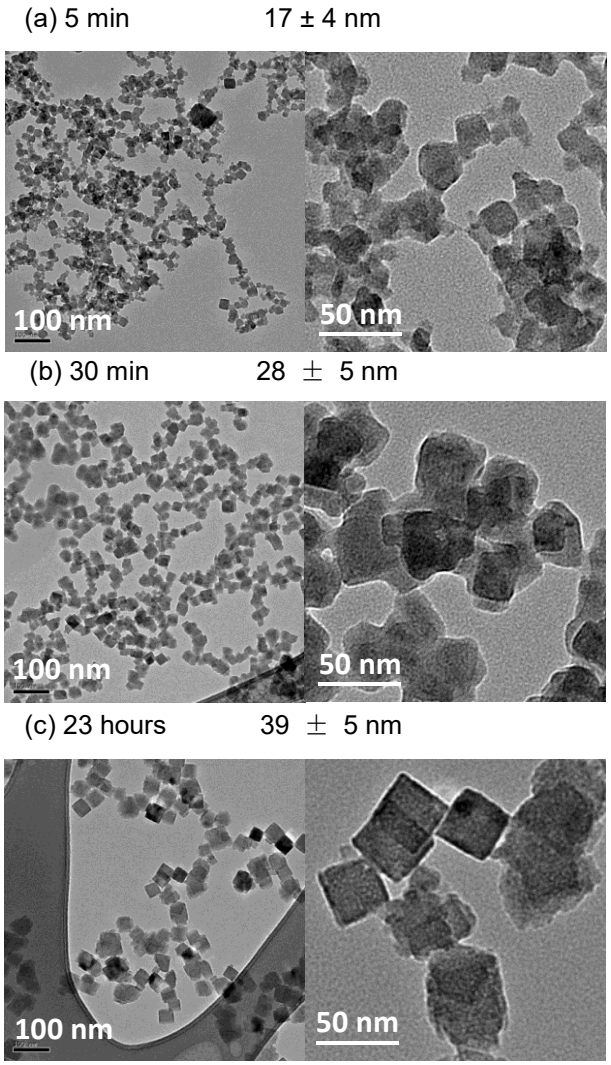

Figure 9. TEM micrographs monitoring the growth of rubidium Prussian blue particles prepared using the slow addition of precursors synthetic method.

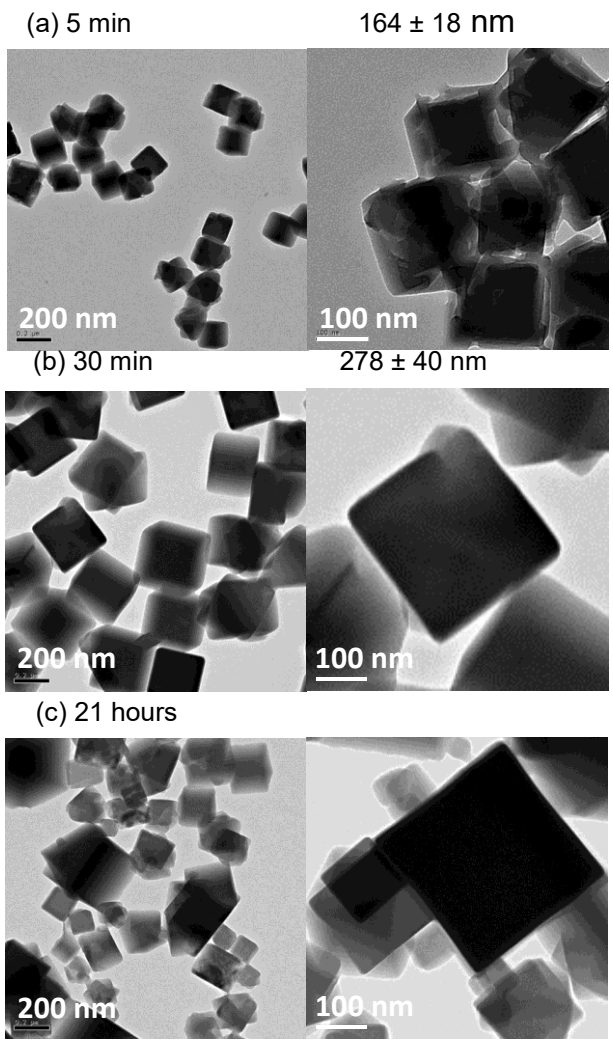

Figure 10. TEM micrographs monitoring the growth of RbCuFe-PBA particles prepared using the slow addition of precursors synthetic method.

The copper hexacyanoferrate also rapidly precipitates. The ionic concentration reaches steady state essentially before the conductance measurement equilibrates (Figure SI17). In contrast to Prussian blue, relatively large particles form immediately with well-defined faces and edges, Figure 10, and there is no evidence for amorphous precursor particles. However, close inspection of the particles at early stages of growth show hollow particles or incompletely formed cubes. Over time, these incomplete particles ripen to fill in the cubes. After 24 hours the ongoing ripening process results in a large particle size dispersion. For copper hexacyanoferrate, though, no precursor particles are observed at any stage, suggesting its growth proceeds by a classical precipitation and ripening process.

Conclusion

Despite the chemical and structural similarities among the 3D Prussian blue analogues, the growth mechanisms of nanoscale and mesoscale crystalline particles can be quite different. On one hand, rubidium copperhexacyanoferrate appears to follow a classical crystal nucleation and growth process where following nucleation ions precipitate and extend the crystallite along well defined crystallographic faces. Subsequent ripening fills in irregular or incomplete shapes which result from the very rapid growth. On the other hand, the rubidium cobalthexacyanometallates grow by a“non-classical” mechanism of aggregation of initially formed precursor particles. Mesoscale particles form by simultaneous addition of nanoscale precursors and annealing or ripening of the aggregates. The rubidium nickelhexacyanometallates resemble more copperhexacyanoferrate in that mesoscale particles grow by a classical heterogeneous precipitation process, although the slower precipitation leads to more uniform particles at each stage of growth. The observations will help inform design and growth strategies in the expanding fields of coordination polymer particles and coordination polymer heterostructures.

Supporting Information.

TEM images and particle size histograms for all samples; time dependence of growth media conductance; and time dependence of DLS response are included.

Conflicts of interest

The authors have no conflicts to declare.

Acknowledgement

We acknowledge the financial support by the National Science Foundation through grants DMR-1904596 and DMR-1405439.

References

(1) Neff, V. D. Electrochemical oxidation and reduction of thin films of Prussian Blue *J. Electrochem. Soc.* **1978**, *125*, 886-887.

(2) Itaya, K.; Uchida, I.; Neff V. Electrochemistry Of Polynuclear Transition-Metal Cyanides - Prussian Blue And Its Analogs. *Acc. Chem. Res.* **1986**, *19*, 162-168.

(3) Nishizawa, M.; Kuwabata S.; Yoneyama, H. Photoimage Formation in a TiO_2 Particle-Incorporated Prussian Blue Film. *J. Electrochem. Soc.* **1996**, *143*, 3462-3465.

(4) Prout, W.; Russell, E.; Groh, H. Ion exchange absorption of cesium by potassium hexacyanocobalt(II) ferrate(II). *J. Inorg. Nucl. Chem.* **1965**, *27*, 473-479.

(5) Vincent, T.; Vincent, C.; Guibal, E. Immobilization of Metal Hexacyanoferrate Ion-Exchangers for the Synthesis of Metal Ion Sorbents-A Mini-Review. *Molecules* **2015**, *20*, 20582-20613.

(6) Schneemeyer, L.; Spengler, S.; Murphy, D. Ion selectivity in nickel hexacyanoferrate films on electrode surfaces. *Inorg. Chem.* **1985**, *24*, 3044-3046.

(7) Pintado, S.; Goberna-Ferron, S.; Escudero-Adan, E.; Galan-Mascaros J. Fast and Persistent Electrocatalytic Water Oxidation by Co-Fe Prussian Blue Coordination Polymers. *J. Am. Chem. Soc.* **2013**, *135*, 13270-13273.

(8) Upadhyay, D.; Gomathi, H.; Rao G.P. Photoelectrochemical properties of Prussian blue-modified glassy carbon. *J. Electroanal. Chem. Interf. Electrochem.* **1991**, *301*, 199-205.

(9) de Tacconi, N. R.; Rajeshwar, K.; Lezna R. O. Metal hexacyanoferrates: electrosynthesis, in situ characterization, and applications. *Chem. Mater.* **2003**, *15*, 3046-3062.

(10) Asakura, D.; Okubo, M.; Mizuno, Y.; Kudo, T.; Zhou, H. S.; Ikedo, K.; Mizokawa, T.; Okazawa, A.; Kojima, N. Fabrication of a Cyanide-Bridged Coordination Polymer Electrode for Enhanced Electrochemical Ion Storage Ability. *J. Phys. Chem. C* **2012**, *116*, 8364-8369.

(11) Asakura, D.; Li, C. H.; Mizuno, Y.; Okubo, M.; Zhou, H.S.; Talham, D. R. Bimetallic Cyanide-Bridged Coordination Polymers as Lithium Ion Cathode Materials: Core@Shell Nanoparticles with Enhanced Cyclability. *J. Am. Chem. Soc.* **2013**, *135*, 2793-2799.

(12) Wessells, C. D.; Huggins, R. A.; Cui, Y. Copper hexacyanoferrate battery electrodes with long cycle life and high power. *Nature Commun.* **2011**, *2*.

(13) Lu, Y. H.; Wang, L.; Cheng, J. G.; Goodenough J. B. Prussian blue: a new framework of electrode materials for sodium batteries. *Chem. Commun.* **2012**, *48*, 6544-6546.

(14) Zhang, K.; Lee, T. H.; Noh, H.; Islamoglu, T.; Farha, O. K.; Jang,H. W.; Choi, J.-W.; Shokouhimehr, M. Realization of Lithium-Ion Capacitors with Enhanced Energy Density via the Use of Gadolinium Hexacyanocobaltate as a Cathode Material. *ACS Appl. Mater. Interfaces* **2019**, *11*, 31799−31805.

(15) Zhang, K.; Lee, T. H.; Noh, H.; Farha, O. K.; Jang,H. W.; Choi, J.-W.; Shokouhimehr, M. Tailorable Topologies for Selectively Controlling Crystals of Expanded Prussian Blue Analogues *Cryst. Growth Des.* **2019**, *19*, 7385−7395.

(16) Verdaguer, M.; Bleuzen, A.; Marvaud, V.; Vaissermann, J.; Seuleiman, M.; Desplanches, C.; Scuiller, A.; Train, C.; Garde, R.; Gelly, G.; Lomenech, C.; Rosenman, I.; Veillet, P.; Cartier, C.; and Villain, F. Molecules to build solids: high T-c molecule-based magnets by design and recent revival of cyano complexes chemistry. *Coord. Chem. Rev.* **1999**, *192*, 1023-1047.

(17) Ohkoshi S. I.; Tokoro, H. Photomagnetism in Cyano-Bridged Bimetal Assemblies. *Acc. Chem. Res.* **2012**, *45*, 1749-1758.

(18) Catala, L.; Mallah, T. Nanoparticles of Prussian blue analogs and related coordination polymers: From information storage to biomedical applications. *Coord. Chem. Rev.* **2017**, *346*, 32-61.

(19) Moulik, S.; De G, Panda, A.; Bhowmik, B.; Das, A. Dispersed molecular aggregates. 1. Synthesis and characterization of nanoparticles of $Cu_2[Fe(CN)_6]$ in H_2O/AOT/n-heptane water-in-oil microemulsion media. *Langmuir* **1999**, *15*, 8361-8367.

(20) Vaucher, S.; Li, M.; Mann S. Synthesis of Prussian blue nanoparticles and nanocrystal superlattices in reverse microemulsions. *Angew. Chemie-Int. Ed.* **2000**, *39*, 1793.

(21) Catala, L.; Gacoin, T.; Boilot, J.; Riviere, E.; Paulsen, C.; Lhotel, E.; Mallah, T. Cyanide-bridged Cr-III-Ni-II superparamagnetic nanoparticles. *Adv. Mater.* **2003**, *15*, 826.

(22) Uemura, T.; Ohba, M.; Kitagawa, S. Size and surface effects of Prussian blue nanoparticles protected by organic polymers. *Inorg. Chem.* **2004**, *43*, 7339-7345.

(23) Zhai, J.; Zhai, Y.; Wang, L.; Dong, S. Rapid synthesis of polyethylenimine-protected Prussian blue nanocubes through a thermal process. *Inorg. Chem.* **2008**, *47*, 7071-7073.

(24) Shen, X.; Wu, S.; Liu, Y.; Wang, K.; Xu, Z.; Liu, W. Morphology syntheses and properties of well-defined Prussian Blue nanocrystals by a facile solution approach. *J. Coll. Interf. Sci.* **2009**, *329*, 188-195.

(25) Chelebaeva, E.; Guari, Y.; Larionova, J.; Trifonov, A.; Guerin, C. Soluble ligand-stabilized cyano-bridged coordination polymer nanoparticles. *Chem. Mater.* **2008**, ***20***, 1367-1375.

(26) Brinzei, D.; Catala, L.; Louvain, N.; Rogez, G.; Stephan, O.; Gloter, A.; Mallah, T. Spontaneous stabilization and isolation of dispersible bimetallic coordination nanoparticles of $Cs_xNi[Cr(CN)_6]_y$. *J. Mat. Chem.* **2006**, *16*, 2593-2599.

(27) Brinzei, D.; Catala, L,; Rogez, G.; Gloter, A.; Mallah, T. Magnetic behaviour of negatively charged nickel(II) hexacyanoferrate(III) coordination nanoparticles. *Inorg. Chim. Acta* **2008**, *361*, 3931-3936.

(28) Catala, L.; Brinzei, D.; Prado, Y.; Gloter, A.; Stephan, O.; Rogez, G.; Mallah, T. Core-Multishell Magnetic Coordination Nanoparticles: Toward Multifunctionality on the Nanoscale. *Angew. Chemie-Int. Ed.* **2009**, *48*, 183-187.

(29) Catala, L.; Volatron, F.; Brinzei, D.; Mallah, T. Functional Coordination Nanoparticles. *Inorg. Chem.* **2009**, *48*, 3360-3370.

(30) Li, C.; Peprah, M.; Asakura, D.; Meisel, M.W ; Okubo, M.; Talham, D. R. Stepwise Reduction of Electrochemically Lithiated Core-Shell Heterostructures Based on the Prussian Blue Analogue Coordination Polymers $K_{0.1}Cu[Fe(CN)_6]_{0.7}3.5H_2O$ and $K_{0.1}Ni[Fe(CN)_6]_{0.7}\cdot 4.4H_2O$. *Chem. Mater.* **2015**, *27*, 1524-1530.

(31) Okubo, M.; Li, C. H.; Talham, D. R. High rate sodium ion insertion into core-shell nanoparticles of Prussian blue analogues. *Chem. Commun.* **2014**, *50*, 1353-1355.

(32) Dumont, M. F.; Knowles, E. S.; Guiet, A.; Pajerowski, D. M.; Gomez, A.; Kycia, S. W.; Meisel, M. W.; Talham, D. R. Photoinduced Magnetism in Core/Shell Prussian Blue Analogue Heterostructures of $K_jNi_k[Cr(CN)_6]_l\ nH_2O$ with $Rb_aCo_b[Fe(CN)_6]_c\ mH_2O$. *Inorg. Chem.* **2011**, *50*, 4295-4300.

(33) Pajerowski D. M.; Gardner, J. E.; Frye, F. A.; Andrus, M. J.; Dumont, M. F.; Knowles, E. S.; Meisel, M. W.; Talham, D. R. Photoinduced Magnetism in a Series of Prussian Blue Analogue Heterostructures. *Chem. Mater.* **2011**, *23*, 3045-3053.

(34) Risset, O. N.; Quintero, P. A.; Brinzari, T. V.; Andrus, M. J.; Lufaso, M. W.; Meisel, M. W.; Talham, D. R. Light-Induced Changes in Magnetism in a Coordination Polymer Heterostructure, $Rb_{0.24}Co[Fe(CN)_6]_{0.74}@K_{0.10}Co[Cr(CN)_6]_{0.70}\,nH_2O$ and the Role of the Shell Thickness on the Properties of Both Core and Shell. *J. Am. Chem. Soc.* **2014**, *136*, 15660-15669.

(35) Risset, O. N; Brinzari, T. V; Meisel, M. W.; Talham, D. R. Light Switchable Magnetism in a Coordination Polymer Heterostructure Combining the Magnetic Potassium Chromiumhexacyanochromate with the Light-Responsive Rubidium Cobalthexacyanoferrate. *Chem. Mater.* **2015**, *27*, 6185-6188.

(36) Felts, A. C., Andrus, M. J.; Knowles, E. S.; Quintero, P. A.; Ahir, A. R.; Risset, O. N.; Li, C.H.; Maurin, I.; Halder, G. J.; Abboud, K. A.; Meisel, M. W.; Talham, D. R. Evidence for Interface-Induced Strain and Its Influence on Photomagnetism in Prussian Blue Analogue Core–Shell Heterostructures, $Rb_aCo_b[Fe(CN)_6]_c{\cdot}mH_2O@K_jNi_k[Cr(CN)_6]_l{\cdot}nH_2O$ *J. Phys. Chem. C* **2016**, *120*, 5420-5429.

(37) Presle, M.; Lemainque, J.; Guigner, J.; Larquet, E.; Maurin, I.; Boilot, J.; Gacoin, T. Controlled growth of core@shell heterostructures based on Prussian blue analogues. *New J. Chem.* **2011**, *35*, 1296-1301.

(38) Presle, M.; Maurin, I.; Maroun, F.; Cortes, R.; Lu, . LL.; Hassan, R. S.; Larquet, E.; Guigner, J. M.; Riviere, E.; Wright, J. P.; Boilot, J. P.; Gacoin, T. Photostrictive/Piezomagnetic Core-Shell Particles Based on Prussian Blue Analogues: Evidence for Confinement Effects? *J. Phys. Chem. C* **2014**, *118*, 13186-13195.

(39) Adam, A.; Poggi, M.; Larquet, E.; Cortes, R.; Martinelli, L.; Coulon, P. E.; Lahera, E.; Proux, O.; Chernyshov, D.; Boukheddaden, K.; Gacoin, T.; Maurin, I. Strain engineering of photo-induced phase transformations in Prussian blue analogue heterostructures. *Nanoscale* **2018**, *10*, 16030-16039.

(40) Dia, N.; Lisnard, L.; Prado, Y.; Gloter, A.; Stephan, O.; Brisset, F.; Hafez, H.; Saad, Z.; Mathoniere, C.; Catala, L.; Mallah, T. Synergy in Photomagnetic/Ferromagnetic Sub-50 nm Core-Multishell Nanoparticies. *Inorg. Chem.* **2013**, *52*, 10264-10274.

(41) Felts, A. C.; Slimani, A.; Cain, J. C.; Andrus, M. J.; Ahir, A. R.; Abboud, K. A.; Meisel, M. W.;

Boukheddaden, K; Talham, D. R. Control of the Speed of a Light-Induced Spin Transition through Mesoscale Core-Shell Architecture. Journal of the American Chemical Society. *J. Am. Chem. Soc.* **2018**, *140*, 5814-5824.

(42) Risset, O. N.; Knowles, E. S.; Ma, S. Q.; Meisel, M. W.; Talham, D. R. $Rb_jM_k[Fe(CN)_6]_l$ (M = Co, Ni) Prussian Blue Analogue Hollow Nanocubes: a New Example of a Multilevel Pore System. *Chem. Mater.* **2013**, *25*, 42-47.

(43) Risset, O. N.; Talham, D. R. Effects of Lattice Misfit on the Growth of Coordination Polymer Heterostructures. *Chem. Mater.* **2015**, *27*, 3838-3843.

(44) Felts, A. C.; Andrus, M. J.; Averback, C. M.; Li, C, H.; Talham, D. R. Comparison of the infrared absorptivities of some Prussian blue analogues and their use to determine the composition of core-shell particles. *Polyhedron* **2017**, *133*, 404-411.

(45) Colfen, H.; Antonietti, M. Mesocrystals: Inorganic superstructures made by highly parallel crystallization and controlled alignment. *Angew. Chemie-Int. Ed.* **2005**, *44*, 5576-5591.

(46) Niederberger, M.; Colfen, H. Oriented attachment and mesocrystals: Non-classical crystallization mechanisms based on nanoparticle assembly. *Phys. Chem. Chem. Phy.* **2006**, *8*, 3271-3287.

(47) Bu, F.; Du, C.; Zhang, Q.; Jiang, J. One-pot synthesis of Prussian blue superparticles from reverse microemulsion. *Crystengcomm* **2014**, *16*, 3113-3120.

(48) Hu, M.; Jiang, J. Non-classical crystallization controlled by centrifugation. *Crystengcomm* **2010**, *12*, 3391-3393.

(49) Zheng, X.; Kuang, Q.; Xu, T.; Jiang, Z.; Zhang, S.; Xie, Z.; Huang, R.; Zheng, L. Growth of Prussian blue microcubes under a hydrothermal condition: Possible nonclassical crystallization by a mesoscale self-assembly. *J. of Phys. Chem. C* **2007**, *111*, 4499-4502.

(50) Hu, M.; Jiang, J.; Lin, C.; Zeng, Y. Prussian blue mesocrystals: an example of self-construction. *Crystengcomm* **2010**, *12*, 2679-2683.

(51) Hu, M.; Ishihara, S.; Ariga, K.; Imura, M.; Yamauchi, Y. Kinetically Controlled Crystallization for Synthesis of Monodispersed Coordination Polymer Nanocubes and Their Self-Assembly to Periodic Arrangements. *Chem.-.Eur. J.* **2013**, *19*, 1882-1885.

For Table of Contents Use Only.

Growth Mechanisms of Mesoscale Prussian Blue Analogue Particles in Modifier-free Synthesis

Jiamin Liang, Carissa H. Li, Daniel R. Talham

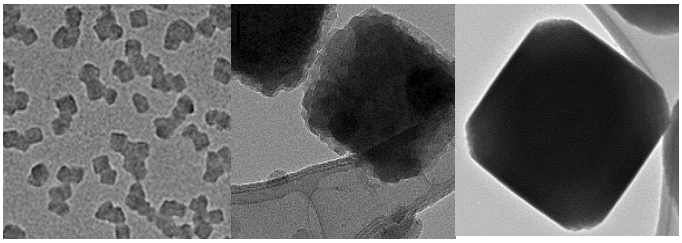

Different growth mechanisms are observed among several members of the Prussian blue analogue family of coordination polymers.

Supporting Information for

Growth Mechanisms of Mesoscale Prussian Blue Analogue Particles in Modifier-free Synthesis

Jiamin Liang, Carissa H. Li, Daniel R. Talham

Department of Chemistry, University of Florida, Gainesville, FL 32611-7200, United States

Corresponding author: Daniel R. Talham

Phone: 352-392-9016

E-mail: talham@chem.ufl.edu

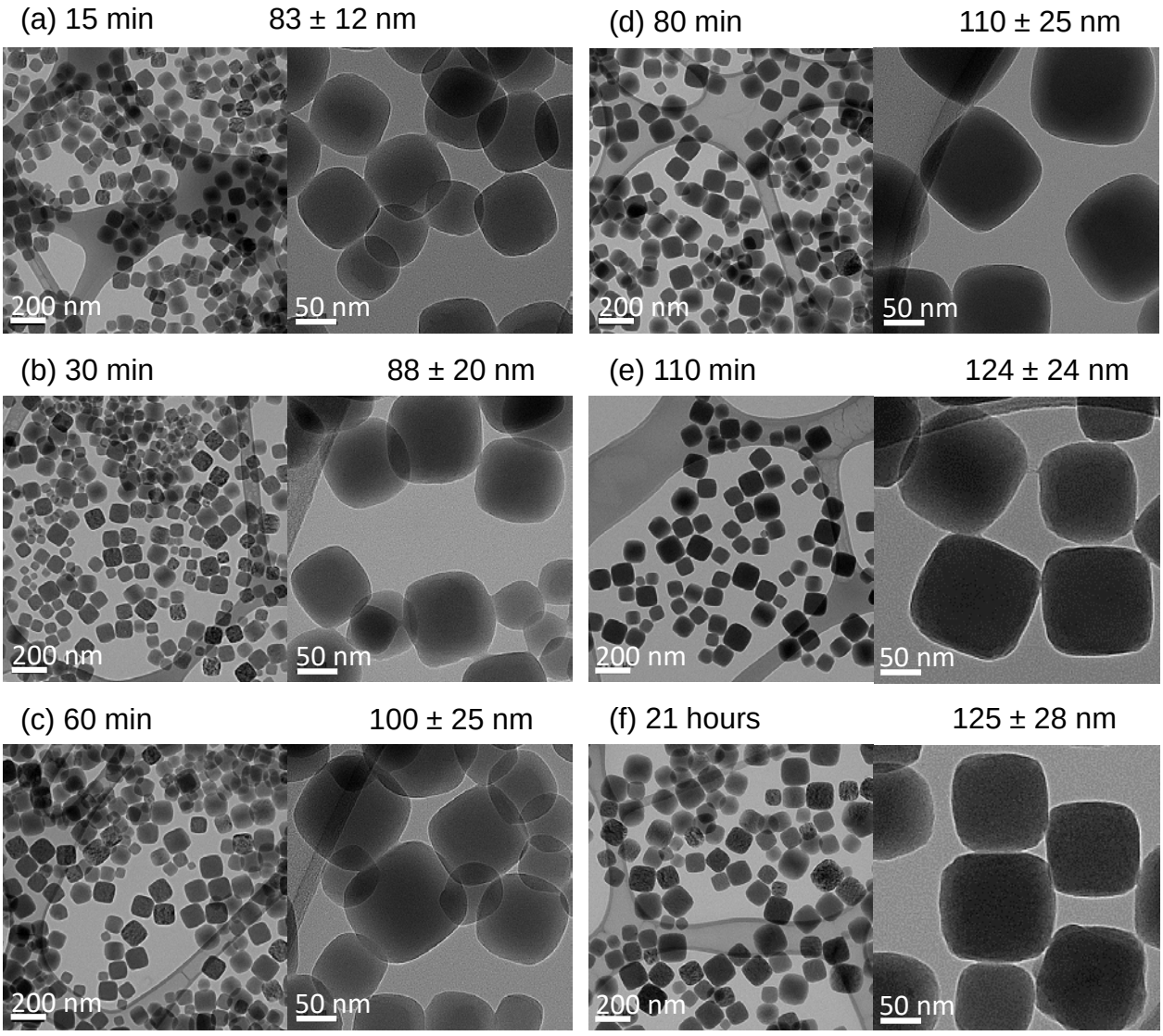

Figure S1. TEM images monitoring the growth of RbNiFe-PBA using the slow-addition synthesis method described in the text. Corresponding particle size histograms are presented in Figure S2.

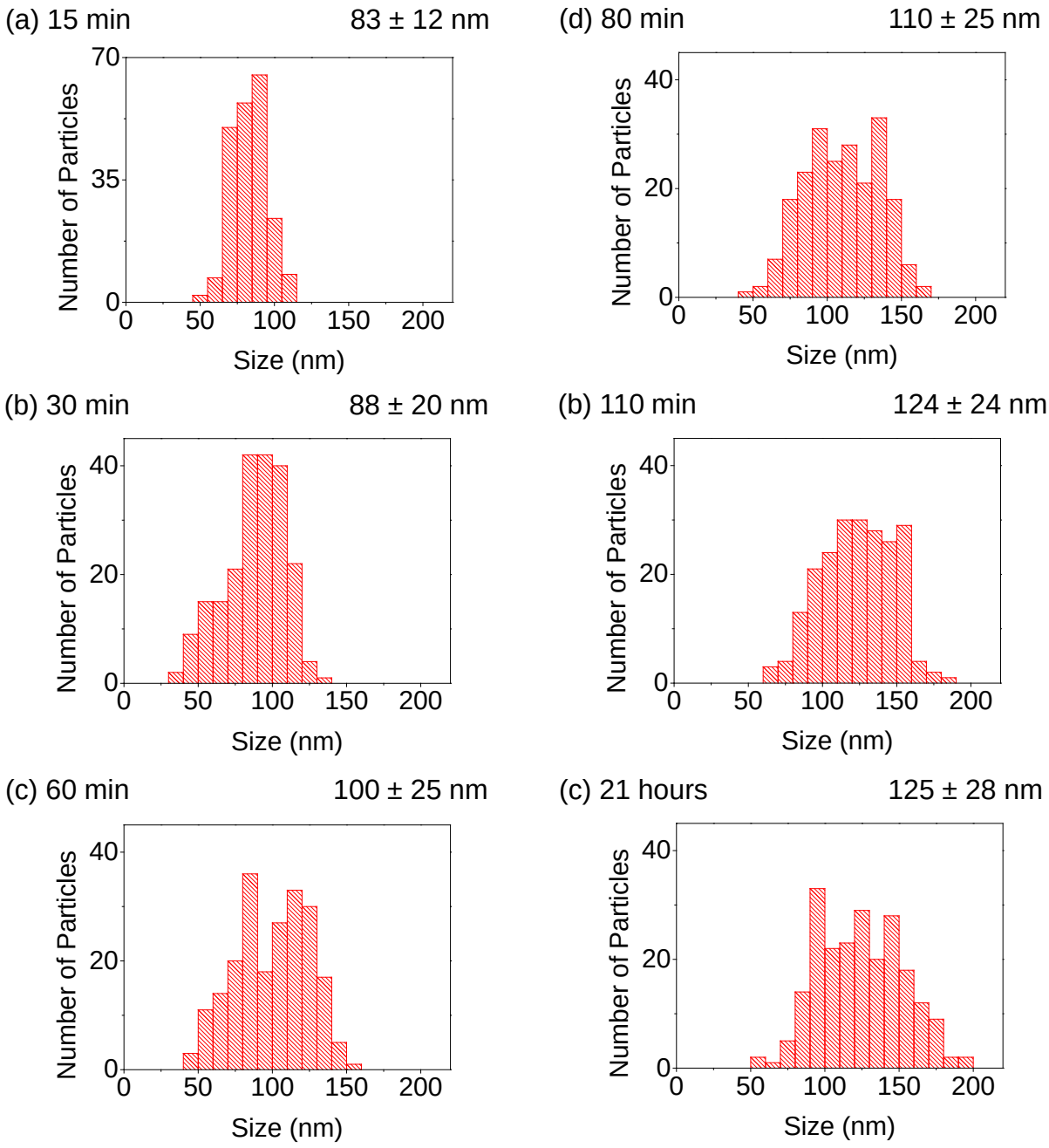

Figure S2. Particle size histograms corresponding to the TEM images in Figure S1.

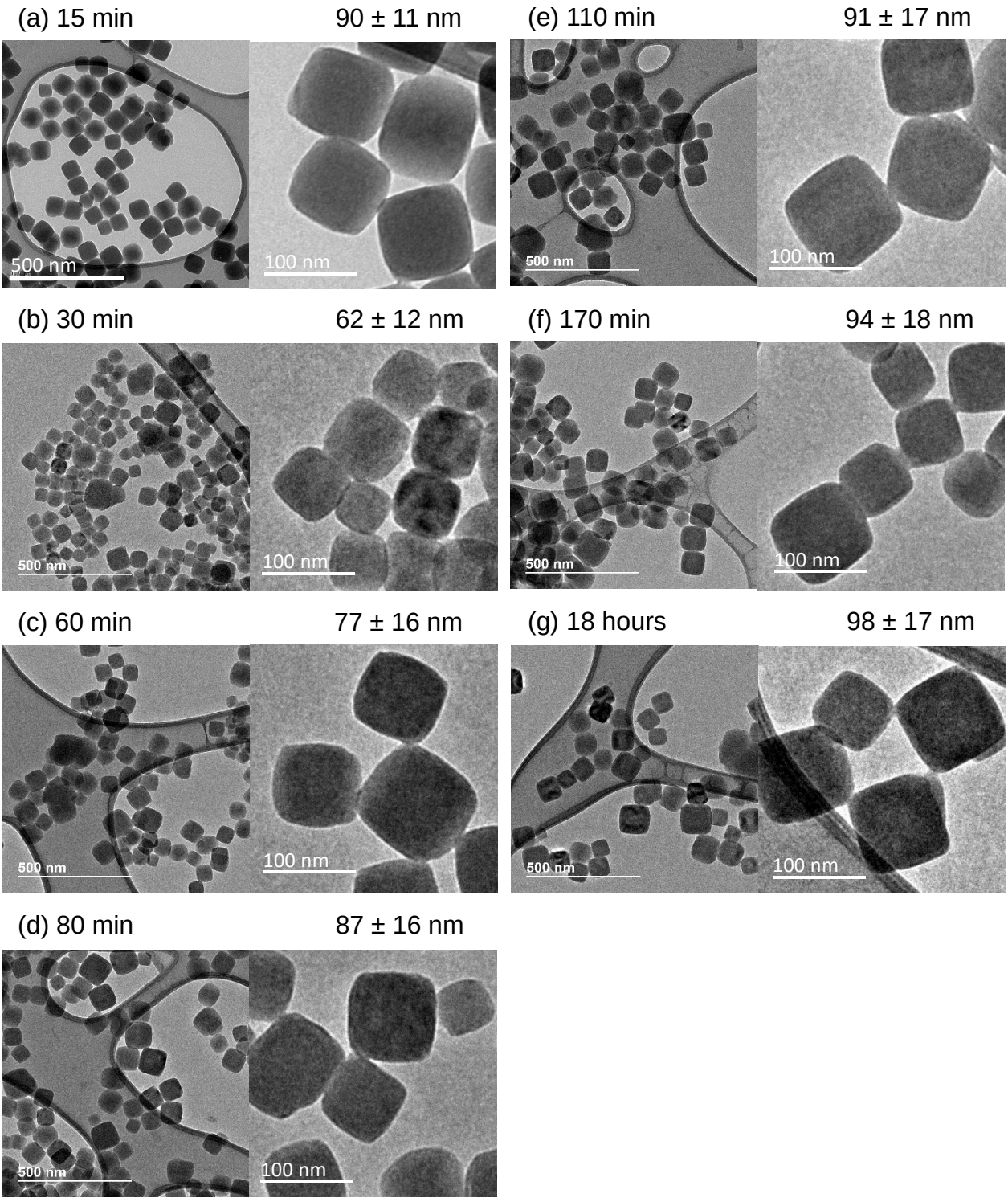

Figure S3. TEM images monitoring the growth of RbNiCr-PBA using the slow-addition synthesis method described in the text. Corresponding particle size histograms are presented in Figure S4.

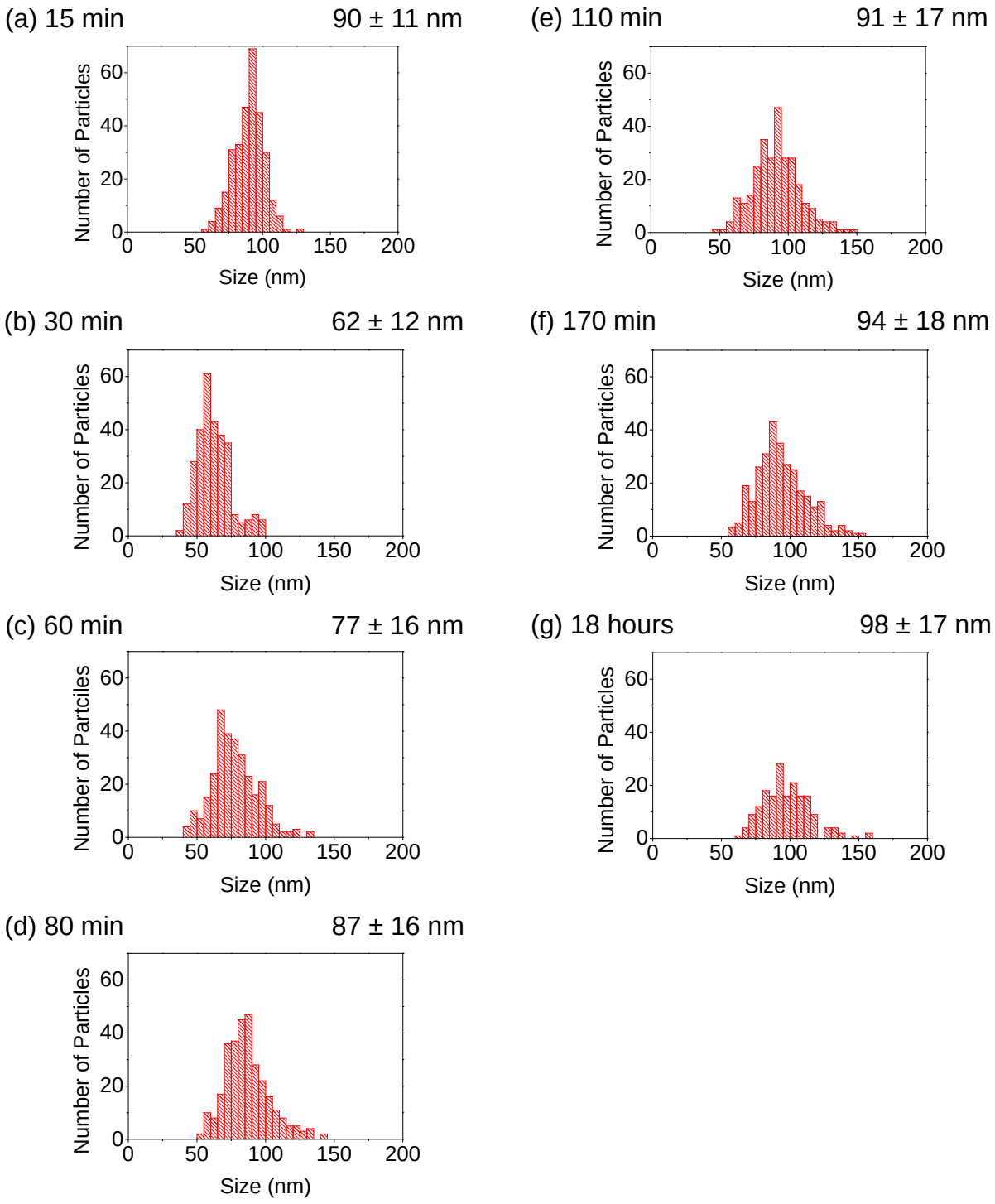

Figure S4. Particle size histograms corresponding to the TEM images in Figure S3.

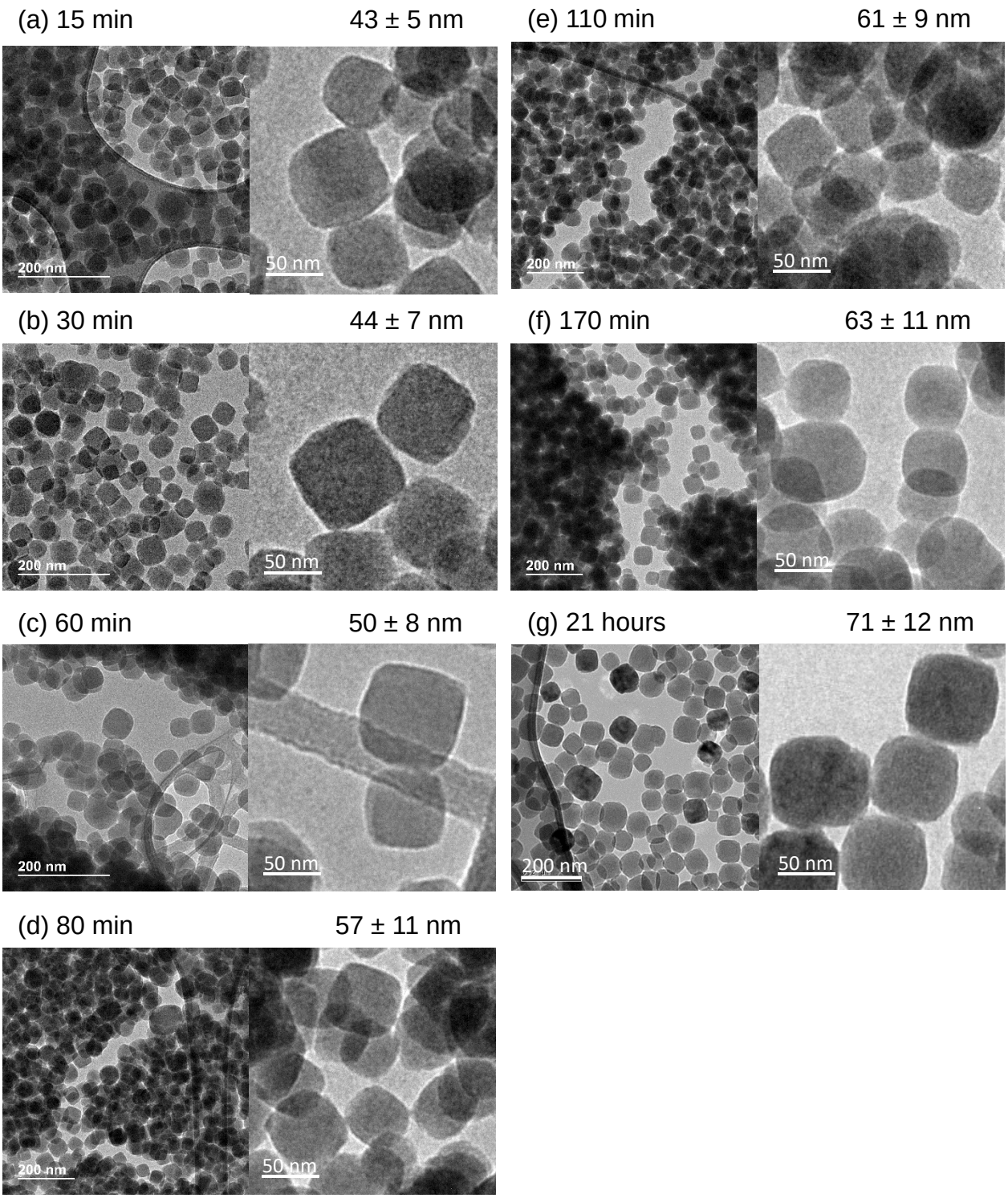

Figure S5. TEM images monitoring the growth of RbNiCo-PBA using the slow-addition synthesis method described in the text. Corresponding particle size histograms are presented in Figure S6.

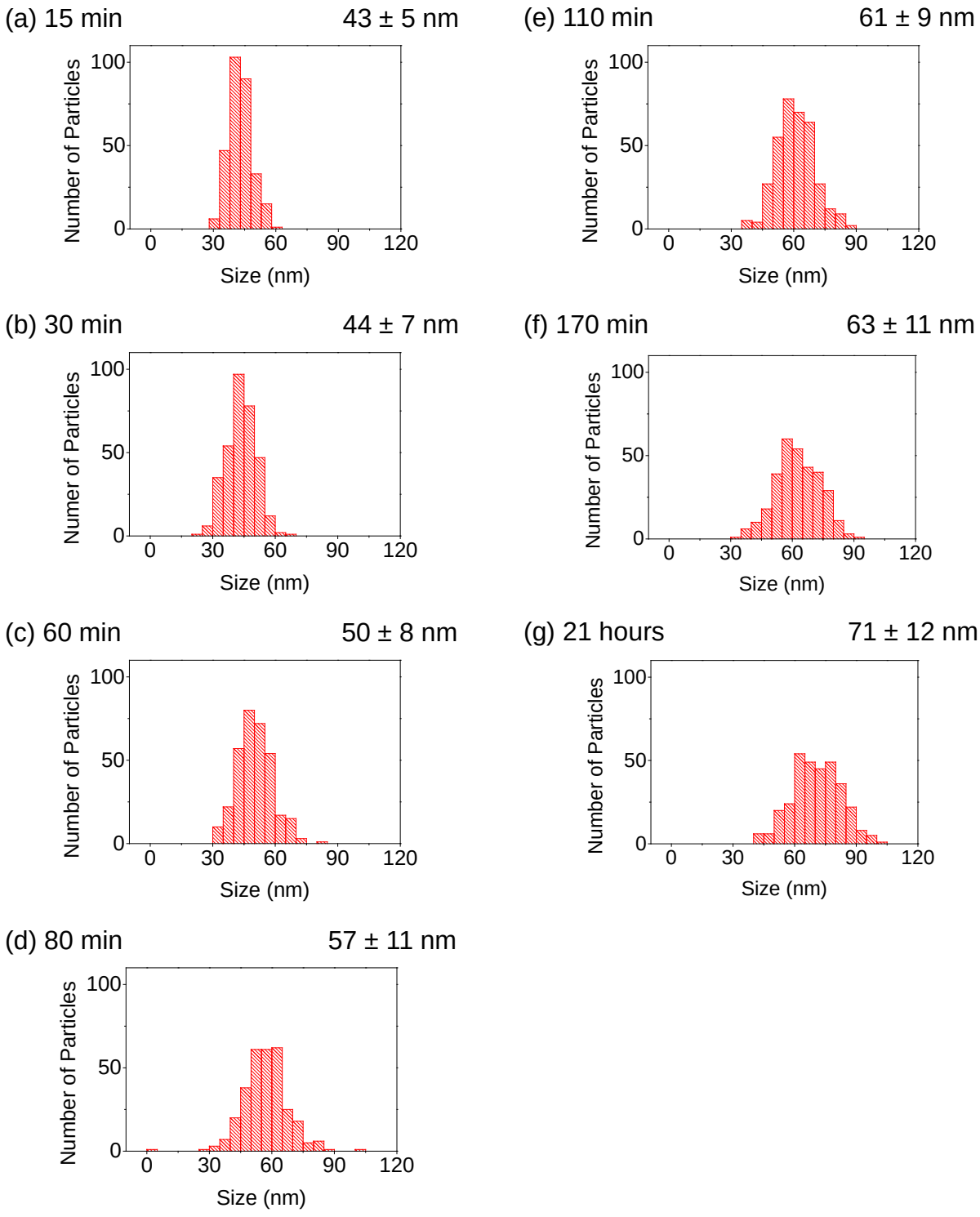

Figure S6. Particle size histograms corresponding to the TEM images in Figure S5.

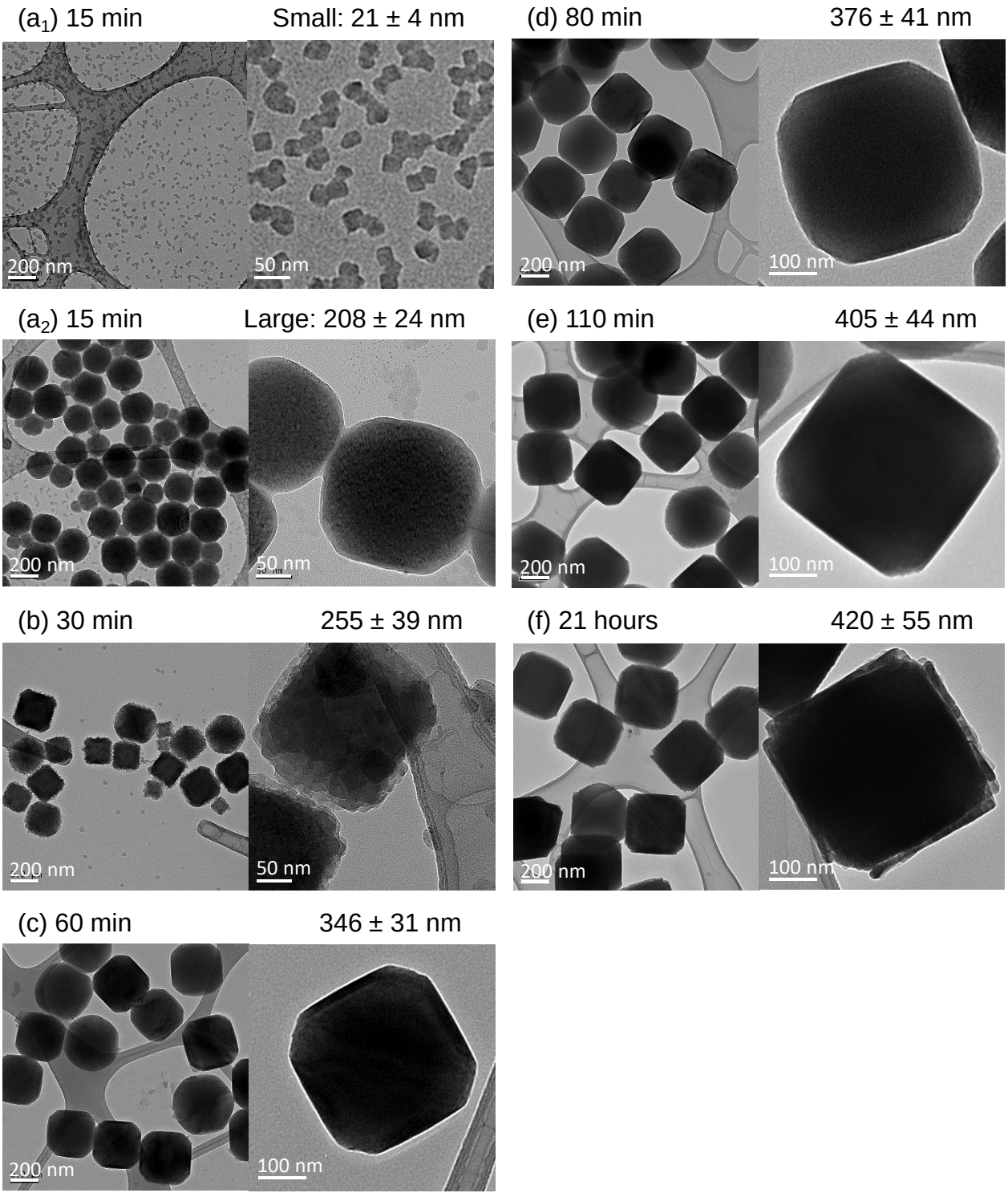

Figure S7. TEM images monitoring the growth of RbCoFe-PBA using the slow-addition synthesis method described in the text. Corresponding particle size histograms are presented in Figure S8.

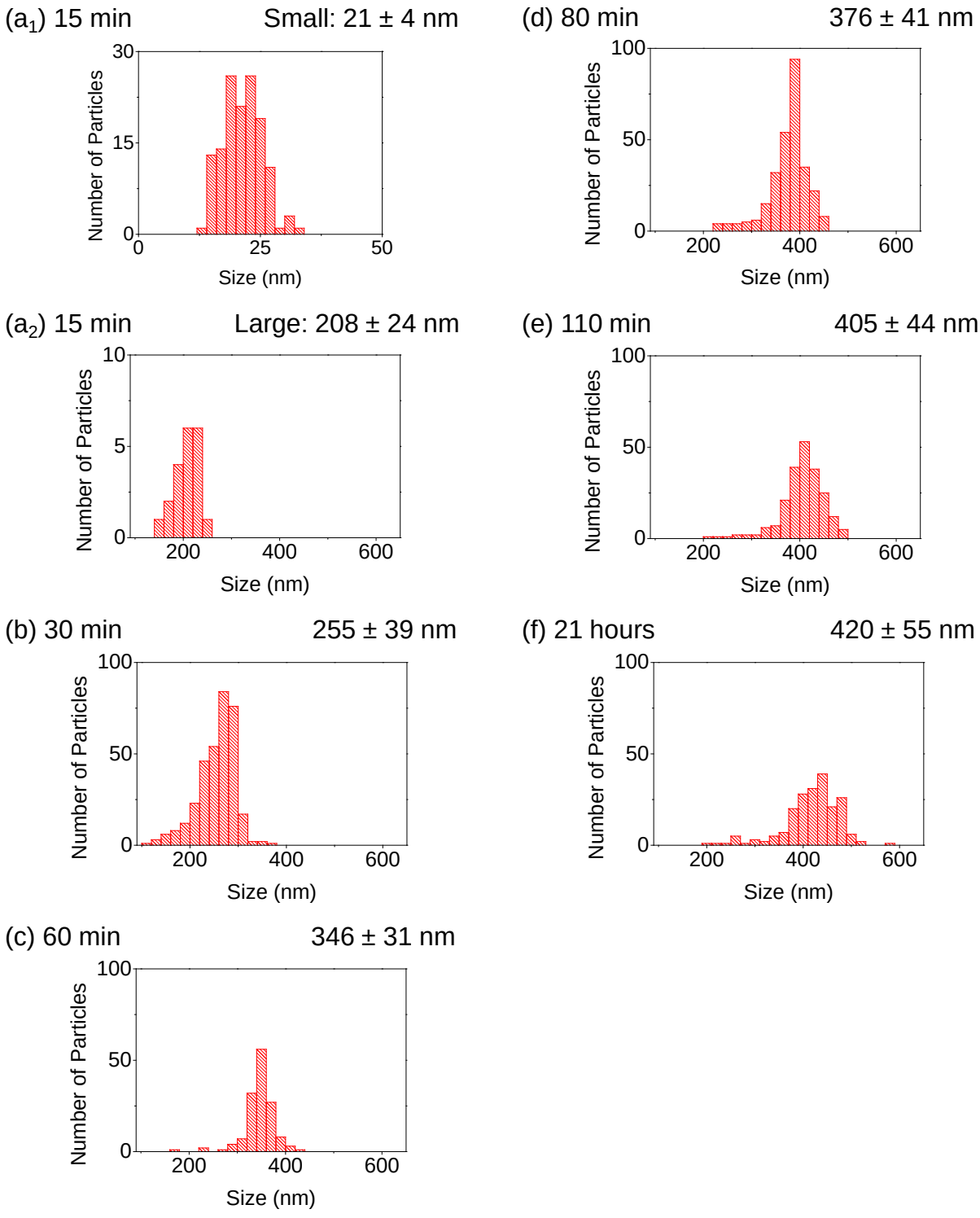

Figure S8. Particle size histograms corresponding to the TEM images in Figure S7.

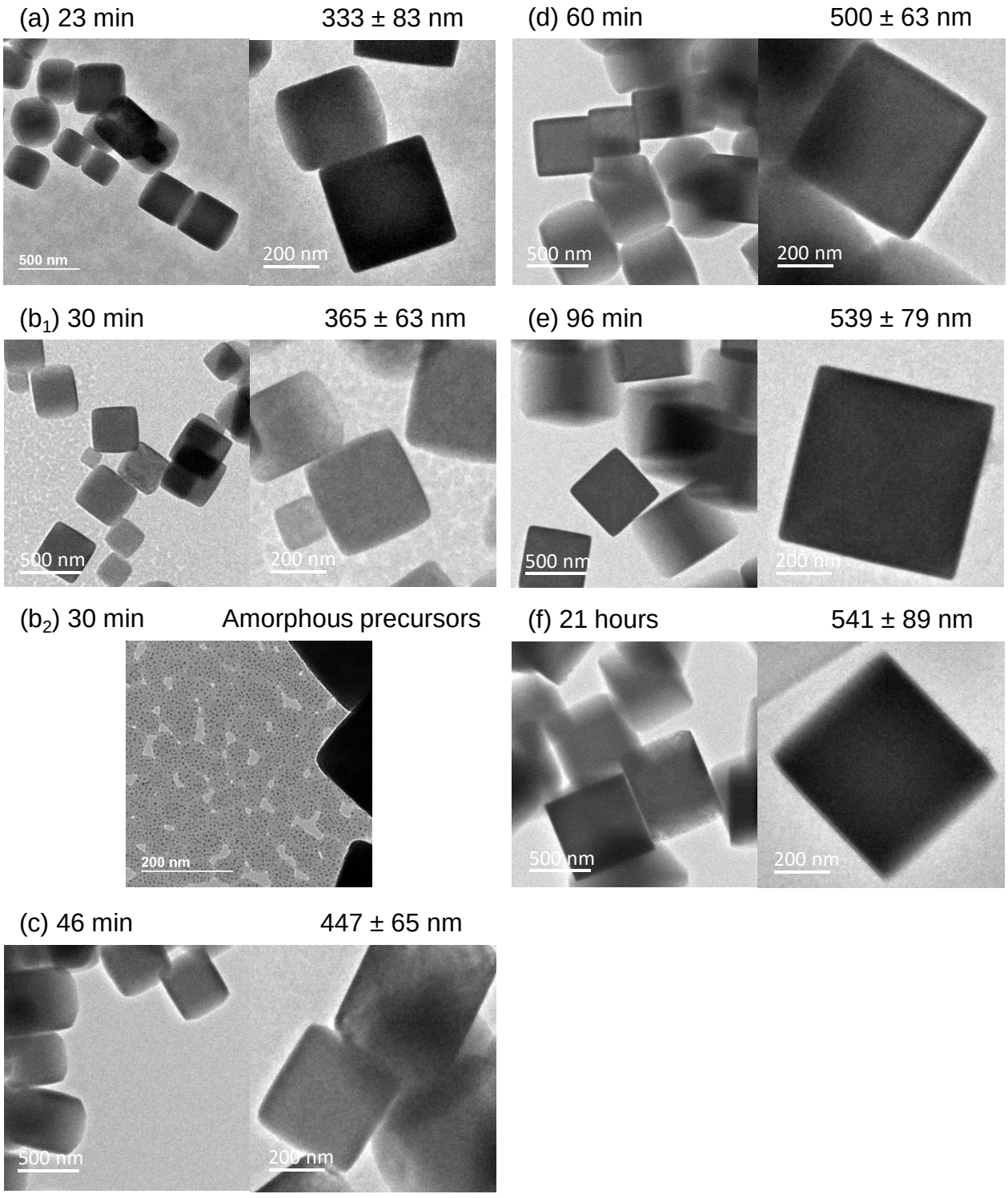

Figure S9. TEM images monitoring the growth of RbCoCr-PBA using the slow-addition synthesis method described in the text. Corresponding particle size histograms are presented in Figure S10.

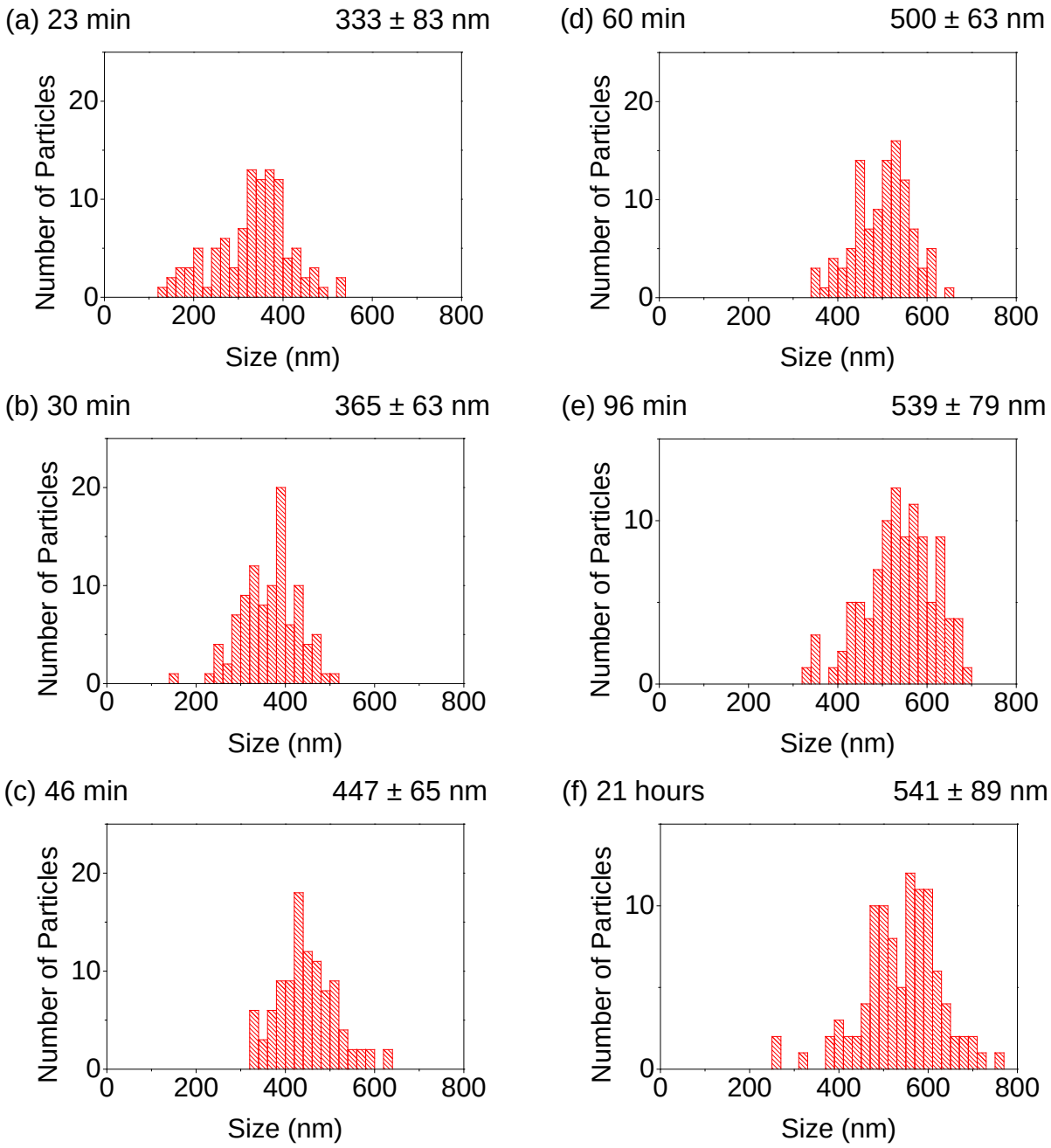

Figure S10. Particle size histograms corresponding to the TEM images in Figure S9.

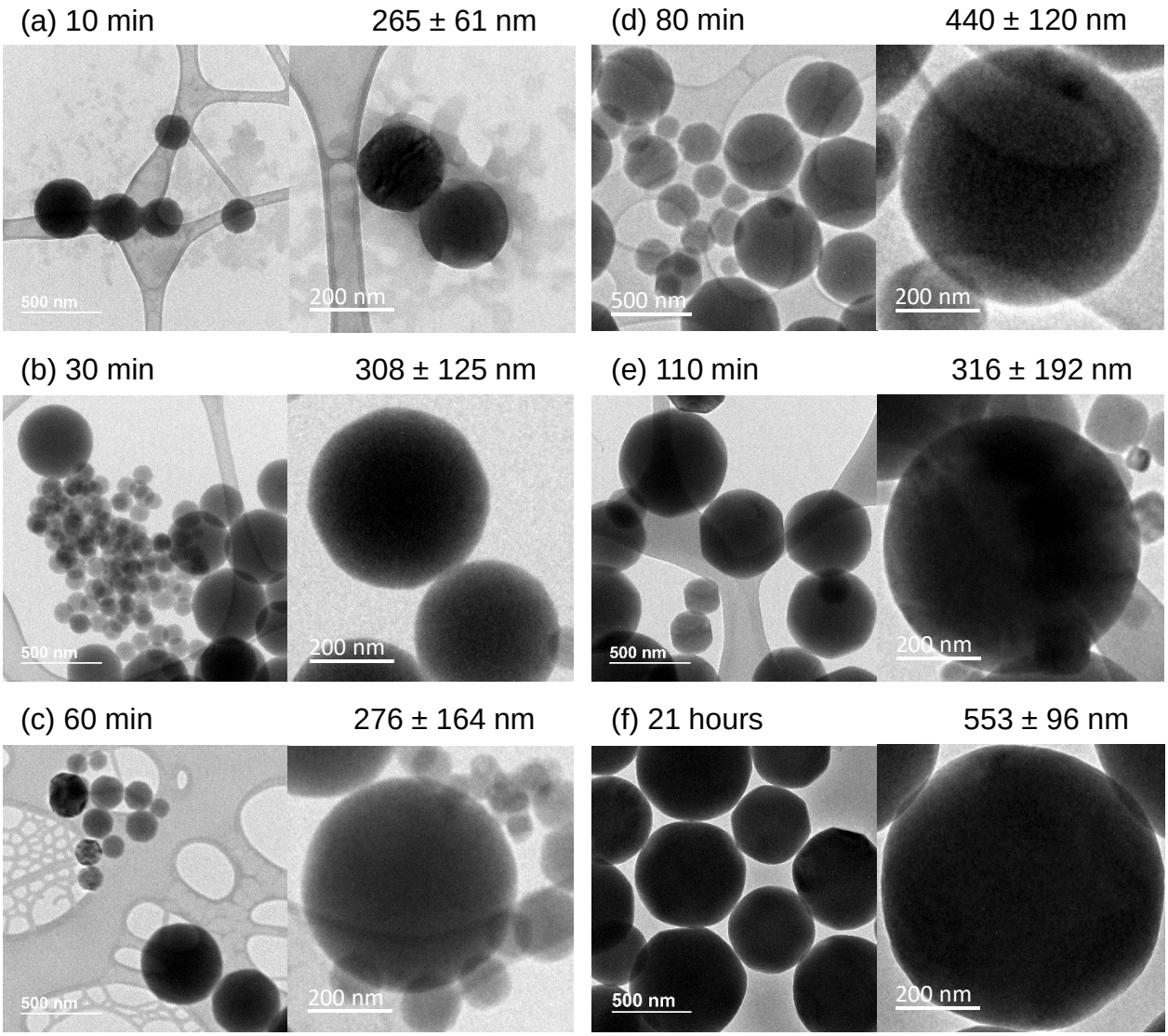

Figure S11. TEM images monitoring the growth of RbCoCo-PBA using the slow-addition synthesis method described in the text. Corresponding particle size histograms are presented in Figure S12.

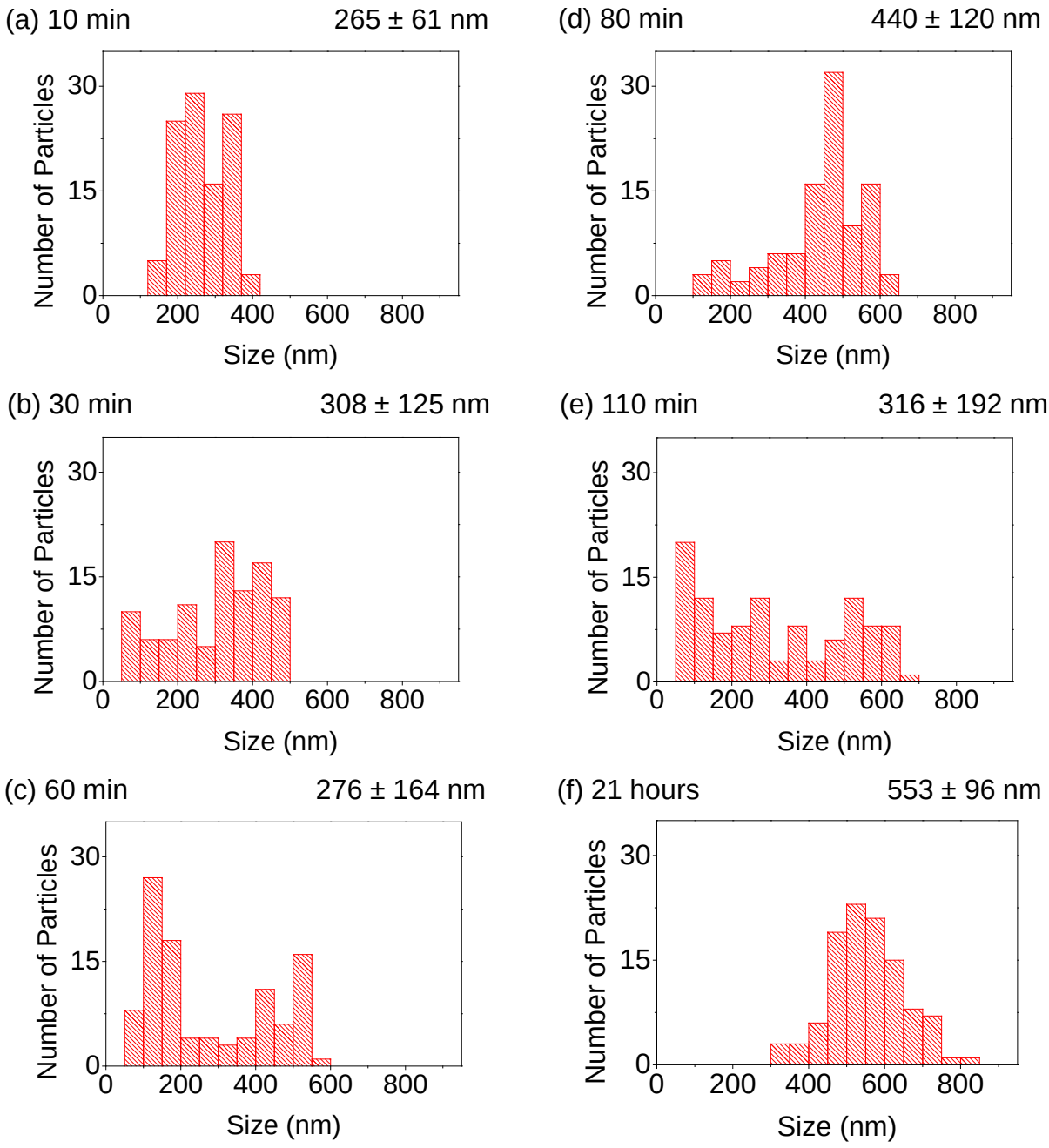

Figure S12. Particle size histograms corresponding to the TEM images in Figure S11.

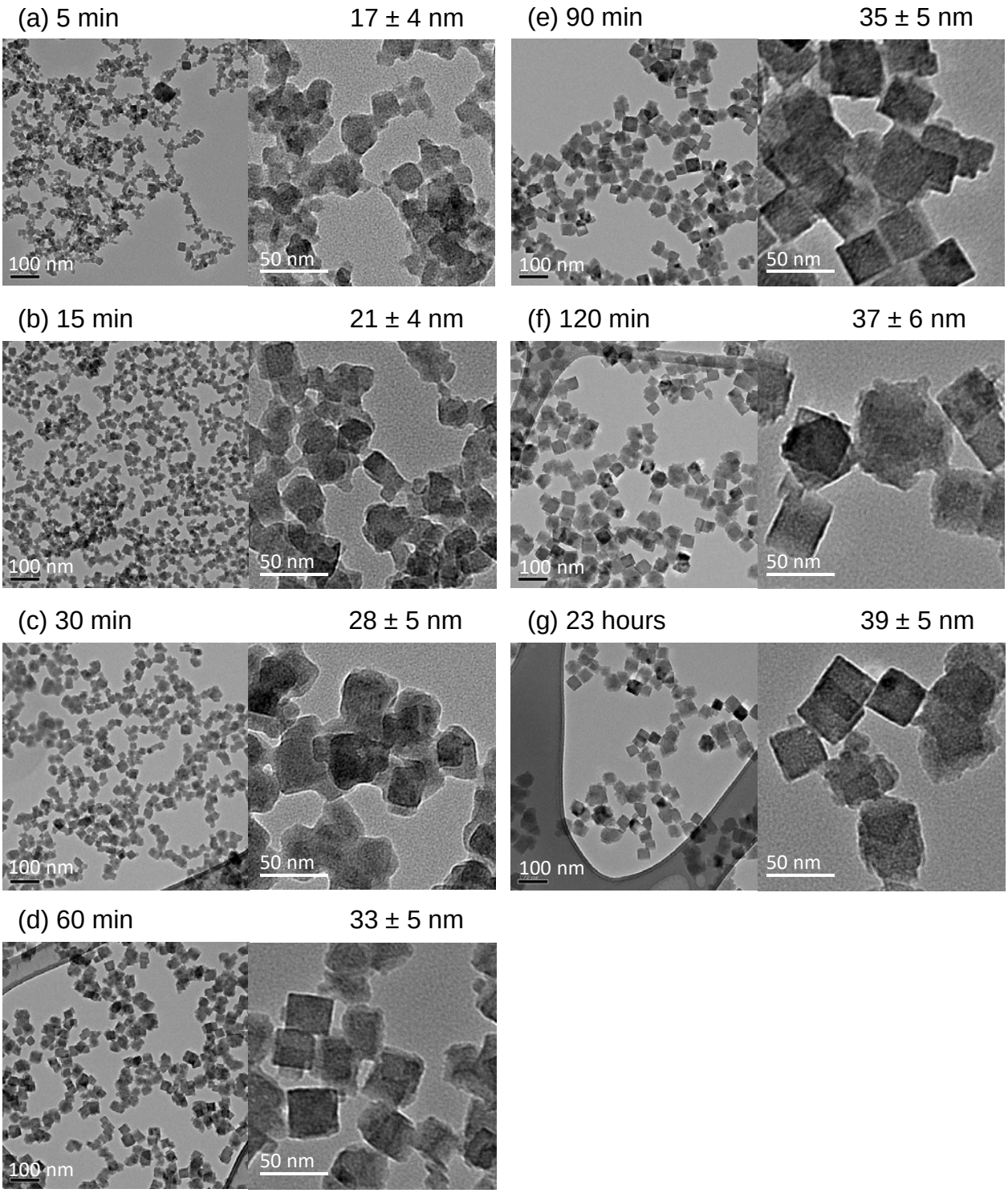

Figure S13. TEM images monitoring the growth of Prussian blue, RbFeFe-PBA, using the slow-addition synthesis method described in the text. Corresponding particle size histograms are presented in Figure S14.

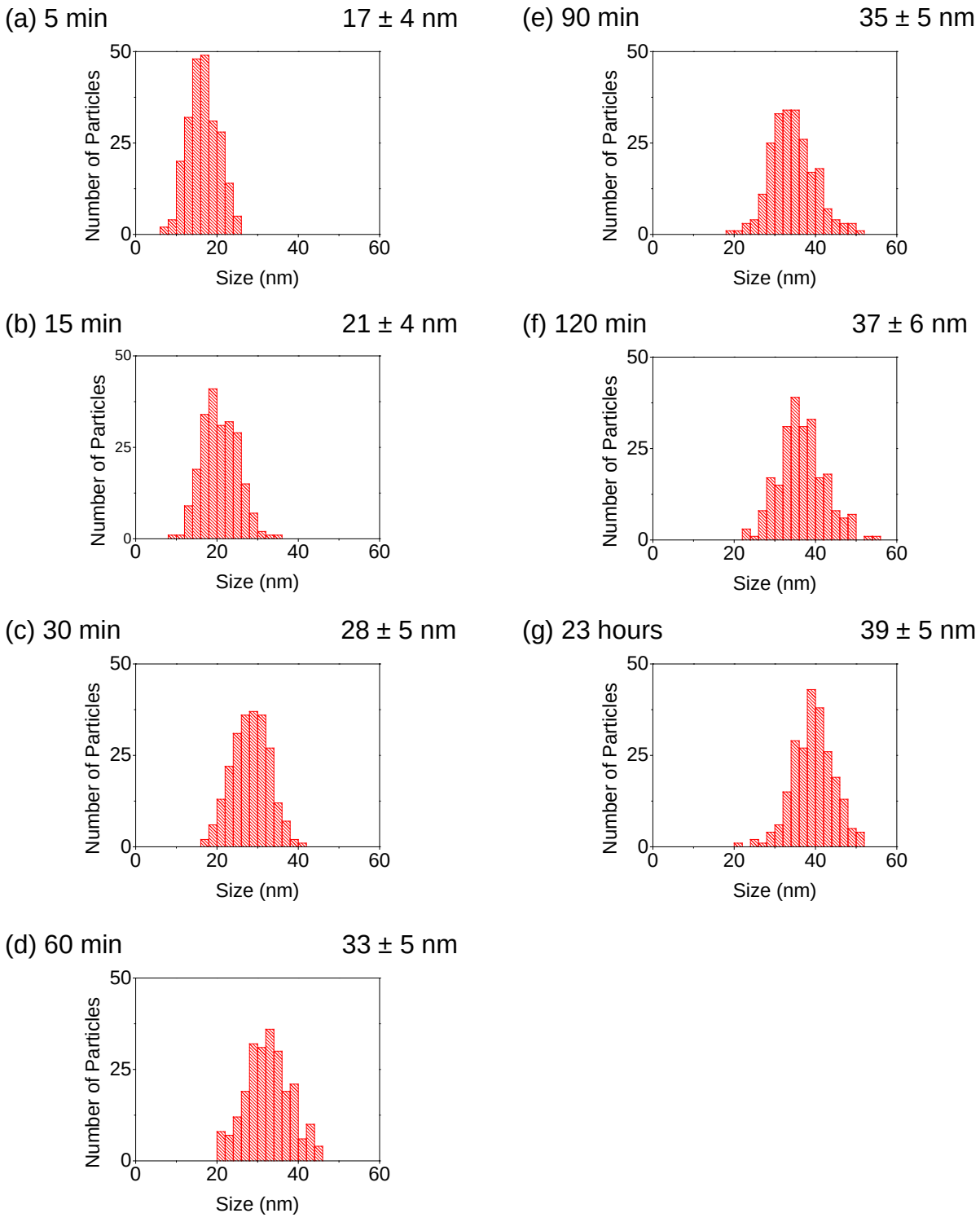

Figure S14. Particle size histograms corresponding to the TEM images in Figure S13.

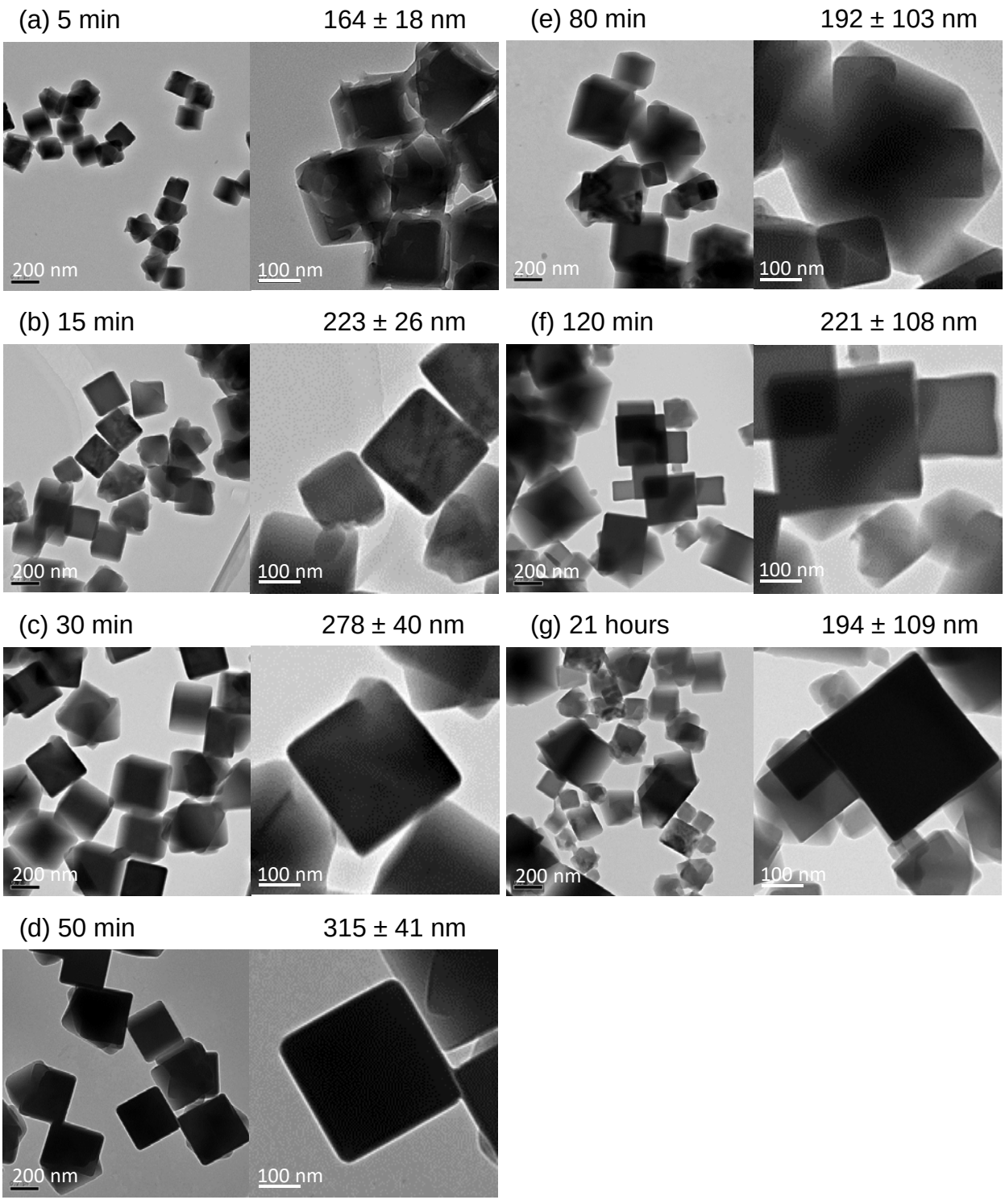

Figure S15. TEM images monitoring the growth of RbCuFe-PBA, using the slow-addition synthesis method described in the text. Corresponding particle size histograms are presented in Figure S16.

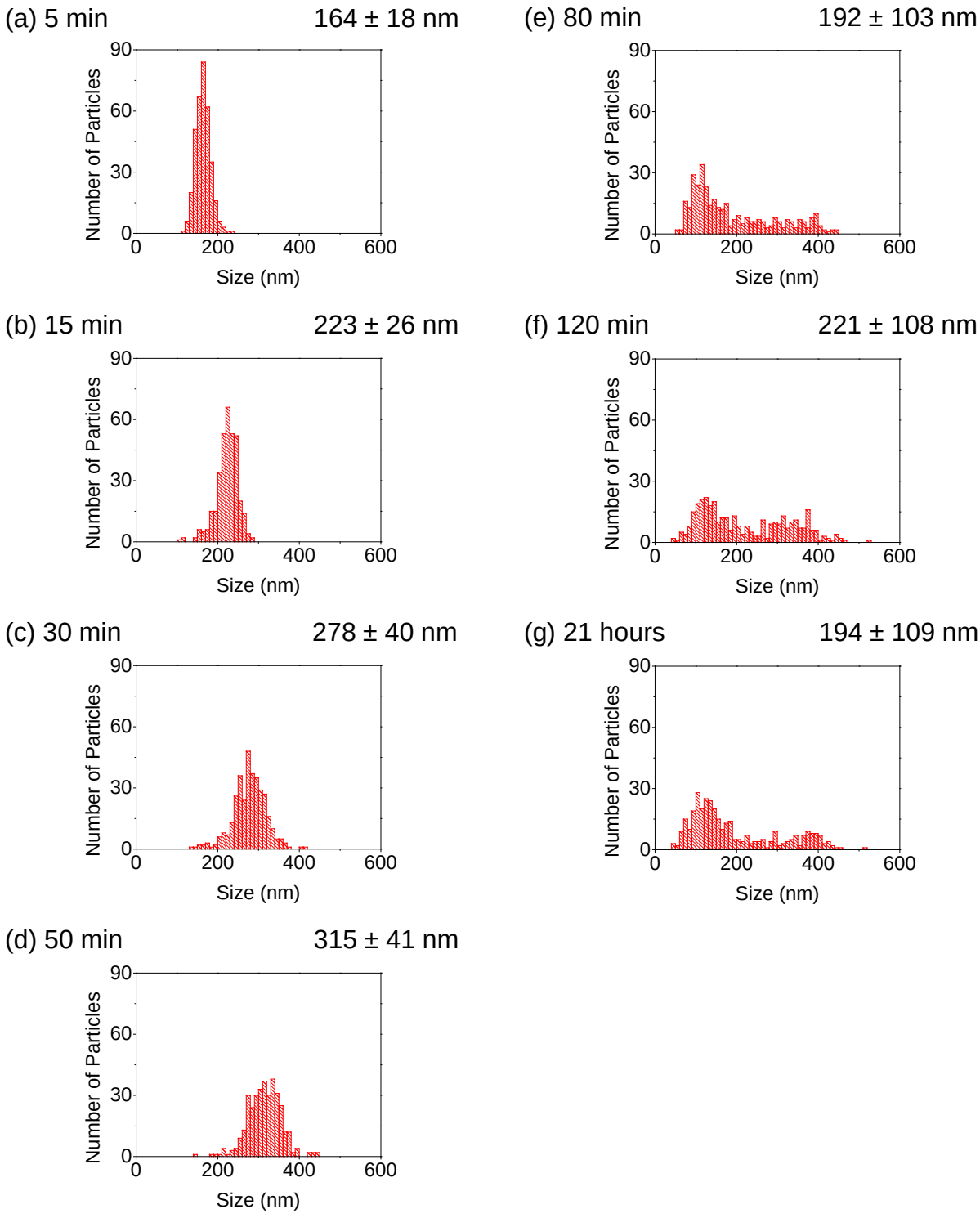

Figure S16. Particle size histograms corresponding to the TEM images in Figure S15.

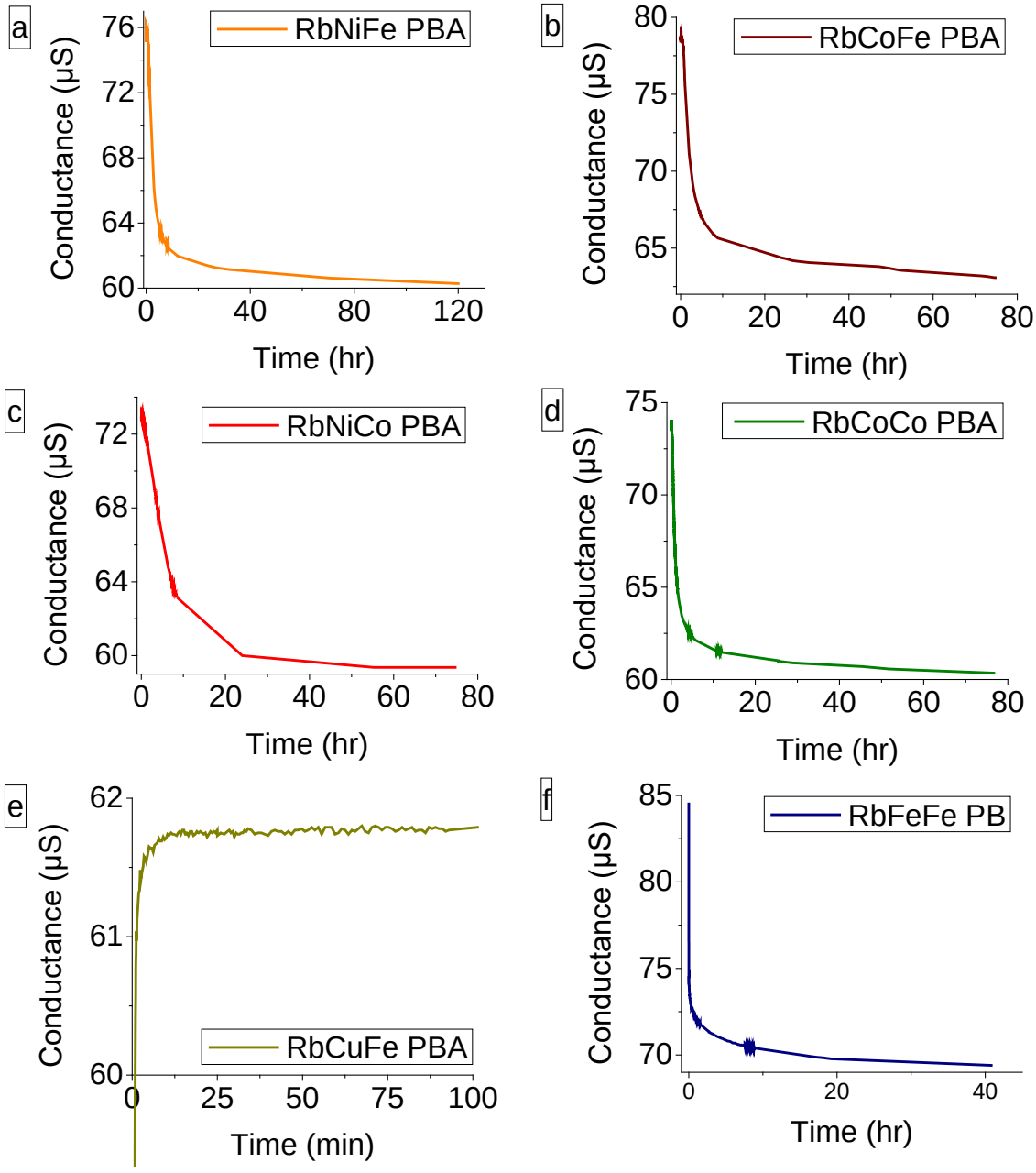

Figure S17. Conductance vs time data monitoring the synthesis of different Prussian blue analogues. The abbreviations correspond to those defined in the text.

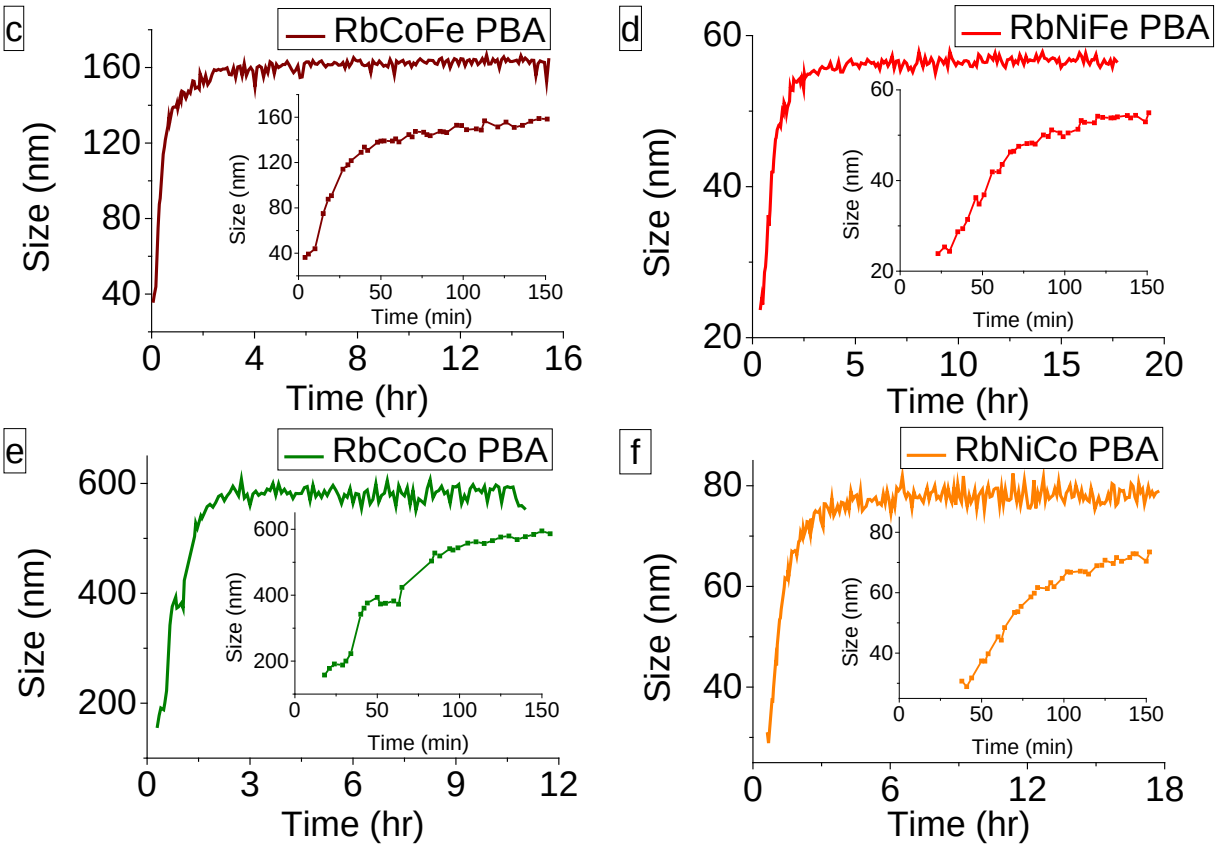

Figure S18. DLS data monitoring the growth of different Prussian blue analogue particles. The abbreviations correspond to those used in the text.